

# CHALMERS

## Towards Improved Scale-Resolving Modeling and Simulations of Turbulent Flows

MAGNUS CARLSSON



THESIS FOR THE DEGREE OF DOCTOR OF PHILOSOPHY IN THERMO AND  
FLUID DYNAMICS

Towards Improved Scale-Resolving Modeling and Simulations of  
Turbulent Flows

MAGNUS CARLSSON

Department of Mechanics and Maritime Sciences  
Division of Fluid Mechanics  
CHALMERS UNIVERSITY OF TECHNOLOGY  
Göteborg, Sweden December 2022

Towards Improved Scale-Resolving Modeling and Simulations of Turbulent Flows  
MAGNUS CARLSSON  
ISBN 978-91-7905-740-4

© MAGNUS CARLSSON, December 2022

Doktorsavhandlingar vid Chalmers tekniska högskola  
Ny serie nr. 5206  
ISSN 0346-718X  
Department of Mechanics and Maritime Sciences  
Division of Fluid Mechanics  
Chalmers University of Technology  
SE-412 96 Göteborg  
Sweden  
Telephone: +46 (0)31-772 1000

Chalmers Reproservice  
Göteborg, Sweden December 2022

Towards Improved Scale-Resolving Modeling and Simulations of Turbulent Flows  
MAGNUS CARLSSON  
Department of Mechanics and Maritime Sciences  
Division of Fluid Mechanics  
Chalmers University of Technology

## ABSTRACT

Scale-resolving simulations are viewed as powerful means for predicting complex turbulent flows, as often encountered in aeronautical applications. However, since turbulent scales span over a considerable range from the smallest Kolmogorov scales to the largest of equivalence to configuration size, scale-resolving computations are often demanding on computational resources and, furthermore, on the underlying numerical methods used in the simulations. Nonetheless, hybrid RANS (Reynolds-Averaged Navier-Stokes)-LES (Large-Eddy Simulation) techniques are considered computationally accurate and affordable for aeronautical industry applications.

This thesis explores and develops numerical methods suitable for hybrid RANS-LES. These methods are implemented in the Computational Fluid Dynamics (CFD) solver M-Edge.

A low-dissipative, low-dispersive numerical scheme was analyzed and verified in subsonic LES of turbulent channel flow and Decaying Isotropic Turbulent (DIT). It was shown that numerical dissipation and dispersion needs to be carefully tuned, in order to accurately predict resolved turbulent stresses and the correct decay of turbulent kinetic energy. The reported results are in good agreement with reference DNS and experimental data. The numerical scheme was further adapted and analyzed for compressible flow, where good agreement with reference DNS and experimental data is achieved for hybrid RANS-LES of supersonic turbulent channel flow and supersonic baseflow.

The optimized numerical scheme was then examined in hybrid RANS-LES computations of developing turbulent channel flow. In order to mitigate the grey area the LES zone, synthetic turbulence was applied at the RANS-LES interface using the Synthetic Eddy Method (SEM) and the Synthetic Turbulence Generator (STG). It was shown that using upstream turbulent statistics from a precursor LES or RANS, the recovery length of the skin friction coefficient can be reduced with improved mitigation of the grey area.

A new implicit gradient reconstruction scheme was developed, which is suitable for node-centered solvers. It was shown that the reconstruction scheme achieves fourth-order scaling on highly irregular anisotropic grids for an analytical academic case.

The Navier-Stokes Characteristic Boundary Condition (NSCBC) was implemented and verified for transport of an analytical vortex. It was shown that special boundary treatment is needed for transporting turbulent structures through the boundary with minimal reflections.

Keywords: Numerical methods, High-order gradient reconstruction, Scale-resolving simulation, Turbulence modelling, Hybrid RANS-LES, Synthetic Turbulence, Compressible flow



*To my family.*



## ACKNOWLEDGEMENTS

I would like to thank my supervisors who gave me the opportunity to pursue a PhD: Lars Davidson at Chalmers, Shia-Hui Peng at FOI and Sebastian Arvidson at Saab Aeronautics. Your support and guidance have been invaluable during the years.

I would like to thank Peter Eliasson and Per Weinerfelt at Saab Aeronautics for providing support regarding the flow solver M-Edge and for the theoretical input on my work. It was always a pleasure to visit you to discuss numerical schemes and discretizations, and mathematics in general. I look forward to continuing the collaboration with you as future colleagues.

I would like to thank all my colleagues at Chalmers for creating an enjoyable work atmosphere. Special thanks to Niklas Hidman for helping me stay in shape by dragging me through the surrounding running trails during lunch breaks in a pace I cannot keep up with, and Gonzalo Montero Villar (Hernandez, Rodriguez, di Maria and all your other family names) for our overlapping work and all interesting discussions we had. I have never enjoyed discussing with someone I have disagreed with this much before.

Furthermore, I would like to thank the following people that I have been in contact with during the PhD: Stefan Wallin at KTH, Stockholm, for showing interest in my work and providing great input and support regarding the length scale based commutation term and turbulence modelling in general. Axel Probst and your colleagues at the German Aerospace Centre (DLR), Göttingen, for having me as a guest researcher May-June 2022. The discussions I had with you regarding numerics, hybrid RANS-LES methods among other things served as a great inspiration and I consider my visit to Göttingen a highlight of my PhD. Alistair Revell at the University of Manchester, for considering having me as a guest researcher in spring 2020. Sadly, a certain pandemic ended those plans.

Finally, I would like to thank my friends and family for the support and especially acknowledge my girlfriend Sara for putting up with my irrational working hours and sometimes lack of acknowledgement.

This work has been funded by the Swedish Governmental Agency for Innovation Systems (VINNOVA), the Swedish Defence Materiel Administration (FMV) and the Swedish Armed Forces within the National Aviation Research Programme (NFFP, Contract No. 2017-04887) and Saab Aeronautics. The simulations were performed on resources provided by the Swedish National Infrastructure for Computing (SNIC) at Chalmers Centre for Computational Science and Engineering (C3SE).

Magnus Carlsson  
Göteborg, December 2022



## NOMENCLATURE

### Greek letters

$\rho$	density
$\sigma_{ij}$	viscous stress tensor
$\mu$	dynamic viscosity
$\nu$	kinematic viscosity
$\Delta$	local filter-width
$\varepsilon$	dissipation rate

### Roman letters

$u_i$	$i^{th}$ component of the velocity vector
$x_i$	$i^{th}$ component of the position vector
$p$	pressure
$e_0$	total energy
$\kappa$	thermal conductivity
$T$	temperature
$C_P$	specific heat at constant pressure
$C_V$	specific heat at constant volume
$R$	universal gas constant
$\gamma$	heat capacity ratio
$P_r$	Prandtl number
$c$	speed of sound
$t_{ij}$	turbulent stress tensor
$k$	turbulent kinetic energy

### Abbreviations

CFD	Computational Fluid Dynamics
NSCBC	Navier-Stokes Characteristic Boundary Condition
RANS	Reynolds Averaged Navier-Stokes
LES	Large Eddy Simulation
ELES	Embedded LES
DNS	Direct Numerical Simulation
HRLM	Hybrid RANS-LES Modeling
STG	Synthetic Turbulence Generator
SEM	Synthetic Eddy Method
DES	Detached Eddy Simulation
(D)DES	Delayed-DES
(I)DDES	Improved-DDES



## THESIS

This thesis consists of an extended summary and the following appended papers:

- Paper A** M. Carlsson, L. Davidson, S.H. Peng, and S. Arvidson. “Investigation of Low-dissipation Low-dispersion Schemes for Incompressible and Compressible Flows in Scale-Resolving Simulations”. Submitted for journal publication
- Paper B** M. Carlsson, L. Davidson, S.H. Peng, and S. Arvidson. “Investigation of Turbulence Injection Methods in Compressible Flow Solvers in Large Eddy Simulation”. *2022 AIAA SciTech Forum*. Jan. 2022. DOI: 10.2514/6.2022-0483
- Paper C** M. Carlsson, L. Davidson, S.H. Peng, and S. Arvidson. “Higher Order Gradients on Unstructured Meshes Using Compact Formulation for Node-Centered Schemes”. *2022 AIAA Aviation Forum*. June 2022. DOI: 10.2514/6.2022-4156
- Paper D** M. Carlsson, S. Wallin, L. Davidson, S.H. Peng, and S. Arvidson. “Seamless Interface Methods for Grey-Area Mitigation in Scale-Resolving Hybrid RANS-LES”. *DLES13 2022*. 2022
- Paper E** M. Carlsson, L. Davidson, S.H. Peng, and S. Arvidson. *Implementation of Nonreflecting Inlet and Outlet Boundary Conditions in the Subsonic Regime for a Node-Based Compressible Solver*. Tech. rep. Chalmers University of Technology, Göteborg, Sweden, Technical Report, 2021

Other publications related to this thesis:

- Paper F** S. Arvidson, M. Carlsson, and S. Nilsson. “Effect of LES Length Scale and Numerical Scheme in Hybrid RANS-LES of Free Shear Layer Flows”. *International Council of Aeronautical Sciences (ICAS), Stockholm*. 2022

## DIVISION OF WORK

All papers were written by M. Carlsson. L. Davidson, S-H. Peng and S. Arvidson provided support and valuable input in the writing and preparation of the manuscripts. L. Davidson has been the main supervisor for this thesis. All implementations of methods in the flow solver M-Edge, simulations, analysis and interpretation of results were performed by M. Carlsson. The development of the numerical scheme presented in Paper A was performed by M. Carlsson, with guidance and support from the co-authors. The formulation of the injection methods in Paper B was done by M. Carlsson with valuable input from S-H. Peng. The implicit gradient reconstruction scheme, presented in Paper C, was derived and developed by M. Carlsson. Theoretical input was provided by S-H. Peng. The stand-alone script for the gradient scheme was written by M. Carlsson. The proposal of the length scale based commutation term in Paper D was formulated by M. Carlsson in collaboration with S. Wallin, where S. Wallin provided theoretical guidance and support. The implementation of the NSCBC in Paper E was done by M. Carlsson.

# CONTENTS

<b>Abstract</b>	<b>i</b>
<b>Acknowledgements</b>	<b>v</b>
<b>Nomenclature</b>	<b>vii</b>
<b>Thesis</b>	<b>ix</b>
<b>Division of Work</b>	<b>x</b>
<b>Contents</b>	<b>xi</b>
<b>I Extended Summary</b>	<b>1</b>
<b>1 Introduction</b>	<b>3</b>
1.1 Modeling of Turbulent Flows . . . . .	3
1.2 Simulation Methods and Accuracy . . . . .	7
1.3 Motivation and Objectives . . . . .	8
<b>2 Modeling of Turbulent Flows</b>	<b>9</b>
2.1 Governing Equations of Fluid Motions . . . . .	9
2.2 Modeling Methodologies . . . . .	10
2.2.1 Reynolds-Averaged-Navier-Stokes (RANS) . . . . .	11
2.2.2 Scale-Resolving Modeling . . . . .	14
2.3 Improvements to Modelling . . . . .	17
2.3.1 LES Length Scale . . . . .	17
2.3.2 Zonal Interface Methods . . . . .	18
2.3.3 Improved Seamless Interface Method . . . . .	23
<b>3 Numerical Methods for Scale-Resolving Simulations</b>	<b>25</b>
3.1 Temporal Discretization . . . . .	25
3.2 Spatial Discretization . . . . .	27
3.2.1 Numerical Dissipation . . . . .	27
3.2.2 Numerical Dispersion . . . . .	29
3.3 Gradient Reconstruction . . . . .	30
3.3.1 Explicit Gradient Reconstruction . . . . .	30
3.3.2 Implicit Gradient Reconstruction . . . . .	31
<b>4 Verification and Validation</b>	<b>33</b>
4.1 Verification and Validation of Numerical Schemes . . . . .	33
4.1.1 Decaying Isotropic Turbulence . . . . .	33
4.1.2 Fully Developed Channel Flow . . . . .	35

4.1.3	Supersonic Baseflow . . . . .	38
4.2	Verification of Gradient Reconstruction . . . . .	41
4.3	Examination of Turbulence Injection Methods . . . . .	43
4.3.1	Spatially Developing Boundary Layer Flow . . . . .	43
4.4	Verification of Seamless GAM Methodology . . . . .	45
4.4.1	Mixing Shear Layer Flow . . . . .	46
<b>5</b>	<b>Summary of Papers</b>	<b>49</b>
5.1	Paper A . . . . .	49
5.2	Paper B . . . . .	50
5.3	Paper C . . . . .	50
5.4	Paper D . . . . .	51
5.5	Paper E . . . . .	52
<b>6</b>	<b>Conclusions and Outlook</b>	<b>55</b>
6.1	Concluding Remarks . . . . .	55
6.2	Outlook . . . . .	56
	<b>References</b>	<b>57</b>
<b>II</b>	<b>Appended Papers</b>	<b>65</b>

# Part I

## Extended Summary

The scope of this thesis is the development of methods used in hybrid RANS-LES modeling. A low-dissipative, low-dispersive numerical scheme is evaluated in Paper A, where it is calibrated and verified in hybrid RANS-LES of turbulent channel flow and Decaying Isotropic Turbulent (DIT). It was concluded that numerical dissipation needs to be carefully reduced, in order to accurately resolve relevant turbulent scales while still achieving a converged solution. The predictions are further improved by the enhanced dispersive properties of the scheme. The numerical scheme was then adopted to and applied in compressible flows, such as a classical shock tube case and in hybrid RANS-LES of supersonic baseflow, where good results with respect to analytical results and experiments are achieved.

In Paper B, an embedded hybrid RANS-LES approach is verified using synthetic turbulence, in order to introduce turbulent fluctuations into a LES domain. Three different methods to inject the synthetic fluctuation into the LES domain was investigated. It was concluded that introducing synthetic fluctuations at the RANS-LES interface can effectively mitigate the grey-area region for turbulent channel flow, where the proposed turbulence injection method gives the best result for developing turbulent channel flow and developing boundary layer flow.

In order to further increase the numerical accuracy, a new implicit gradient reconstruction scheme was proposed in paper C. The reconstruction scheme achieves fourth-order scaling on irregular, highly anisotropic mixed-element grids for an analytical academic case.

In Paper D, a new seamless hybrid RANS-LES approach was derived and evaluated for free shear layer flows. The method exploits the commutation error at RANS-LES interfaces, where a commutation error term based on the hybrid length-scale is applied to reduce the grey-area in the vicinity of the RANS-LES interface. Improved results with respect to experiment are achieved in hybrid RANS-LES of mixing shear layer flows.

To avoid nonphysical reflections in scale-resolving simulations, the boundaries of a truncated flow domain needs to be able to handle incoming and outgoing numerical or physical waves. The Navier-Stokes Characteristic Boundary Condition (NSCBC) was implemented and verified for transporting an analytical vortex through the boundaries in paper E.

This thesis is organized as follows. An introduction is given Chapter 1 where hybrid RANS-LES methods are introduced with an aeronautical perspective. A survey of turbulent inflow boundary conditions is given, along with numerical methods commonly used in hybrid RANS-LES. The turbulence modeling approaches and the numerical methods used in this thesis are presented in Chapters 2 and 3, respectively. Chapter 4 further validates the turbulence modeling approaches and numerical methods used for additional test cases. A summary of the appended papers is given in Chapter 5. Finally, Chapter 6 summarizes the outcomes of the thesis work.



# Chapter 1

## Introduction

Aviation industries have over the years made tremendous effort dedicating to innovation and development of technologies in order to reduce environmental footprint with reduced life-cycle costs of aeronautical systems. Computer-based techniques, which have been increasingly implemented to support aircraft design and performance analysis, have shown great potentials in supplementing costly wind-tunnel and flight tests. Indeed, multi-disciplinary design optimization is now becoming possible in industrial applications, by incorporating model-based tools/approaches in design procedure, and advanced flow simulation strategies in performance analysis. The techniques as such have been implemented in research and development of novel and innovative aeronautical products to support the realization of the targets in line with e.g. ACARE 2020 [1] and FlightPath 2050 [2].

In conjunction with different functionalities, Computational Fluid Dynamics (CFD) form the core and the fundamental platform of flow simulations. To address turbulent flows commonly encountered in aeronautical applications, the methods used today for aerodynamic design are mainly based on steady-state RANS (Reynolds-Averaged Navier-Stokes) simulations, which often provide reliable results for steady flows and attached boundary layers. In dealing with complex aerodynamic flows characterized by, for example, massive flow separation and unsteady vortex motion, RANS methods become often inaccurate. In many applications, resolved turbulence is required to support reliable analysis of, e.g., aeroacoustic noise generation. Obviously, it is desirable to introduce accurate and reliable modelling and simulation methods, such as advanced turbulence modelling and improved numerical schemes, in order to enable scale-resolving simulations in an industrial environment. It is recognized that, by definition, spectral effects are lost in Reynolds-averaging of conventional RANS methods, which are unable to produce scale-resolving predictions. On the other hand, the use of LES (Large-Eddy Simulation) methods remains unfeasible in complex aeronautical applications in the foreseeable future. As highlighted in the NASA CFD vision [3], nonetheless, Hybrid RANS-LES and wall-modeled LES offers the best prospects for industry applications.

With improved flow simulation techniques, accurate predictions of complex unsteady fluid flows can be made, i.e. separated flows which can lead to system disturbances and structural fatigue. Hybrid RANS-LES techniques are considered to be sufficiently accurate and computationally affordable for the aeronautical industry. Industrially adapted hybrid RANS-LES modelling (HRLM) techniques thus have the potential to improve product quality, give a more efficient design process with shorter time-to-market for new products and products with a reduced environmental impact.

### 1.1 Modeling of Turbulent Flows

Turbulence is a three-dimensional, chaotic and unsteady phenomenon governed by the Navier-Stokes equations. It is present in most flows in nature and in engineering applications, for example, the flows around cars, airplanes, trains as well as and flows in a

ventilated room or in a combustion chamber. Turbulence appears when the inertial force dominates significantly over the viscous force, which are characterized by high Reynolds numbers. Its chaotic nature makes it difficult to estimate or solve analytically, and often numerical simulations are required. Turbulent flows are considered to consist of swirling structures of different sizes, which are usually referred to as eddies.

These eddies are characterized by three different scales: a length scale, a time scale and a velocity scale. The kinetic energy of these eddies can be statistically quantified by studying the energy spectrum illustrated in Fig. 1.1, where the energy of eddies with a certain length scale is described by the inverse of their length scale, the wave number  $\kappa \propto 1/l$ .

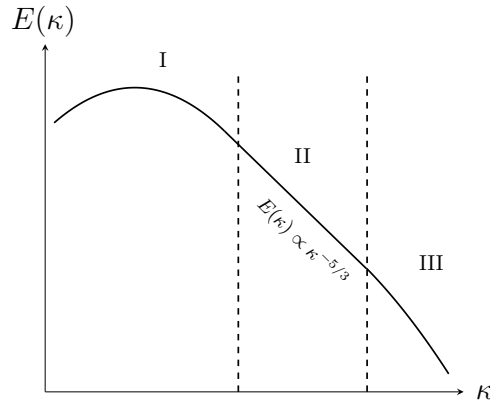


Figure 1.1: *Energy spectrum. I: Large scale energy containing eddies, II: Inertial subrange and III: Dissipative range.  $E(\kappa)$  is the turbulent kinetic energy and  $\kappa$  is the wave number.*

The energy spectrum is divided into three sub-regions. Eddies in region I shown in Fig. 1.1 are the most energy-containing eddies and extract energy from the mean flow. They have a length scale proportional to the geometry of the problem being studied, but are unstable and will eventually break down into smaller eddies. Part of the energy extracted from the largest scales is transferred to the smaller scales. This process is repeated and the energy transfer to the smaller scales is referred to as the cascade process.

Eddies in region II (presented in Fig. 1.1), the inertial sub-range, have become statistically isotropic, i.e. they have no preferred direction, and exhibits a  $\kappa^{-5/3}$  decay in the energy spectrum. The eddies located in the dissipative range, indicated by region III in Fig. 1.1, are described by the Kolmogorov scales. Here, the turbulent kinetic energy is transferred to thermal heat through viscous dissipation. Energy conservation dictates that the energy dissipation from the small eddies to heat in region III must be in the order of the rate of energy transfer from large eddies in region I.

The complex non-linear interaction described above is reflected by turbulence modeling. The common techniques in turbulence modeling are presented in Fig. 1.2, where the region resolution of the corresponding modeling technique is indicated in the turbulent kinetic energy spectrum. Different modeling techniques aim to model and/or resolve different parts of the spectrum. Direct numerical simulation (DNS) is the most accurate

method available for investigating fundamental physics of turbulent flows. In DNS, the Navier-Stokes equations are solved numerically without any turbulence model. This gives an exact solution of the flow field in time and space. However, in order to resolve all the turbulent scales, the local grid size and time step need to be in the order of the Kolmogorov scales. This is extremely costly in terms of computer resources for domains with large dimensions or at large Reynolds number, and this approach currently remains out of reach for most engineering applications.

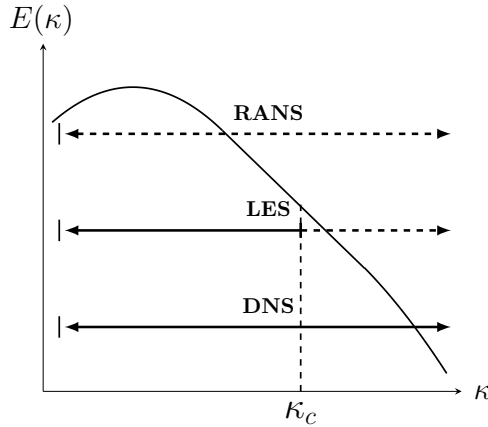


Figure 1.2: *Spectrum for turbulent kinetic energy. Turbulence modeling techniques are indicated with horizontal lines, where dashed indicates modeled part and solid indicates resolved part. Vertical dashed line indicates the location of the cut-off frequency  $\kappa_c$ .*

The computational methods associated with the lowest computational cost, but the least general method, is the RANS family, which model all turbulent scales by Reynolds-averaging the Navier-Stokes equations. The time-averaging needs to be sufficiently large in comparison with the turbulent time scale. Of different RANS methodologies, the most commonly used are eddy viscosity based models (EVM), which approximate the turbulent stresses using a linear relation of the mean strain-rate tensor and an eddy viscosity, and Reynolds stress models (RSM), in which aims to either solve the transport equations for the turbulent stresses or to formulate the turbulent stress tensor in a non-linear algebraic form. RANS models work well in flows where the time variation in the mean flow is of much lower frequency than the turbulence itself, but may fail when the mean flow quantities are strongly affected by large scale turbulent eddies.

Different from RANS, LES methods are based on the spatial filtering of the Navier-Stokes equations. LES aims to model the effect of sub-grid small scales that are more isotropic, while the large scale motions are explicitly computed. The spatial filtering introduces a cut-off frequency  $\kappa_c$ , as indicated in Fig. 1.2, which is inversely proportional to the local cell size  $\Delta$ . The small scales are commonly described as Sub-Grid-Scales (SGS), and the filter-width should be chosen so that  $\kappa_c$  is in the inertial sub-range (see region II in Fig. 1.1) for accurate LES predictions. Compared to the full statistical averaging in RANS, the LES resolves the large scale turbulent interactions, and information about

velocity, pressure fluctuations as well as e.g. two-point correlations are possible to obtain. However, while being much more computationally affordable than DNS, LES suffer from the requirement that the near-wall energetic eddies to a large part need to be resolved, which is still beyond the realistic computational limit for most engineering applications.

## Hybrid RANS-LES modeling

Due to the excessive computational demand by LES and DNS, common practices for CFD-based workflows in the aeronautical industry still utilize steady RANS, although HRLM are increasingly adopted for certain classes of simulations in which swirling and separated flows are dominant. The key feature of HRLM is the RANS-type behavior in the vicinity of a solid boundary and a LES-type behavior joint with the RANS-modelled wall layer. In the HRLM framework, the most commonly used methods include the family of detached eddy simulation (DES) [4, 5, 6], which was extended by boundary-layer shielding, e.g. delayed DES (DDES) [7] and further wall modelling improvements in the improved DDES (IDDES) [8]. The DES-type of methods blend between the different modes through a hybrid length scale, which is adapted to the RANS length scale in the RANS region and to the LES length scale in the LES region. Alternative HRLM includes the partially integrated transport modeling (PITM) method [9, 10], the partially averaged Navier-Stokes (PANS) method [11, 12], and the scale adaptive simulation (SAS) [13]. Unlike in DES, the PANS formulation introduces a resolution parameter in terms of the ratio between the modeled and the total turbulent kinetic energy (resolved plus modeled). Another HRLM is for example the algebraic HYB0-model [14, 15], which blends between a mixing-length RANS model and a Smagorinsky LES model through an empirical blending function.

In embedded LES (ELES) or other zonal hybrid RANS-LES approaches a LES zone, embedded in the RANS region, is introduced to resolve the turbulent flow in regions of particular interest. The aim is to increase accuracy and to reduce the computational effort. The Zonal Detached Eddy Simulation (ZDES) [16, 17] is an example of such approaches. In connection to the RANS-modelled turbulence feeding into the LES region at the RANS-LES interface, the resolved turbulence in the LES region neighboring the interface is often delayed. This is the so-called "grey-area problem", which is not only present in zonal modeling approaches but also in non-zonal hybrid RANS-LES computations as well.

In LES, when the Navier–Stokes equations are subjected to spatially varying filter widths, it is recognized that the filtering operation and the standard finite volume spatial discretization does not commute [18], i.e. one introduces extra error terms called commutation errors. It was also shown in the hybrid RANS-LES context that these commutation residues may be potentially significant in regions with a filter width varying between RANS and LES scales [19, 20], which may further delay the transition from RANS to LES. In the PANS context, these commutation errors were explicitly accounted in simulations with temporal resolution variation [21], which was shown to promote the production of resolved turbulence. This was further investigated in [22, 23, 24], where the commutation residue term is active between the RANS and LES regions over and prescribed interface. It has been proven that that the commutation residue term can significantly accelerate the transition from modeled to resolved turbulence.

## 1.2 Simulation Methods and Accuracy

### Synthetic Turbulence

The grey-area problem can be further mitigated by introducing resolved turbulence based on the statistics of the upstream modeled RANS turbulence. The most general approach is to synthesize artificial turbulence based on turbulent length scales and time scales from the mean RANS flow field using a so-called synthetic turbulence generator (STG). An ideal STG should be able to inject turbulent structures that are realistic for the specific problem under study. This involves satisfying the desired mean velocity profile, Reynolds stress tensor, turbulent kinetic energy spectrum, and correct phase information [25].

A family of STG methods attempt to synthesize a turbulent velocity field through the use of a spectral approach [26], where the fluctuating velocity field is represented by a Fourier series expansion. The intensity of the fluctuations can be computed from a modified von Karman spectrum and second-order statistics can be imposed through a Cholesky-decomposition-based tensor scaling approach [27, 28]. Temporal correlation of the fluctuation may be imposed by applying a time-filter [29] or a modified position vector scaled with the bulk velocity of the flow [28].

Another family of approaches is the Synthetic Eddy methods (SEM) [30, 31], where the turbulent field is superimposed by virtual vortical structures. These vortical structures or eddies are randomly generated and convected through a fictional domain, usually taken a box, giving both spatial and temporal correlation to the fluctuations, which are allowed to induce perturbations to cells in their neighbourhood. The SEM is able to predict statistical input data but fails to reproduce realistic spectral properties and yields a fluctuating velocity field with non-zero divergence [32]. Improvement was made to the original SEM, by which it was extended to give a divergence-free (DF-SEM)[32] fluctuating velocity field, and a generalization of the fictional domain in order to remove the dependency of the box [33], simplifying the implementation for complex geometries.

### Numerical Accuracy

Proper resolution of the LES mode in HRLM requires a minimal dissipative and minimal dispersion numerical scheme. In scale-resolving computations, the accuracy and the order of the numerical method dictates the capabilities of resolving relevant length and time scales for turbulent flows, where higher-order methods (higher than second-order) are popular. Higher-order methods can be achieved by increasing the discretization stencil with additional neighbor points or by assuming a high-order polynomial for each cell. For complex geometries, which are typical for problems in the aeronautical applications, unstructured grids are often used to provide a quick discretization of the flow domain. For an unstructured flow solver, managing this type of grids poses a severe challenge due to the fact that the cells can have arbitrary shape and number of neighbours. Examples of higher-order methods for unstructured grids are higher-order finite-volume [34, 35], discontinuous galerkin [36], spectral volume [37, 38] or spectral difference [39, 40]. For an industrially capable CFD-package using second-order schemes, incorporating the changes adapting to higher-order methods require often substantial changes.

A low-dissipative finite-volume scheme suitable for unstructured compressible solvers was developed by Probst et al. [41], where the added numerical dissipation was effectively reduced and demonstrated with improved turbulence-resolving capabilities for wall-bounded flows. To further improve the capabilities of the numerical scheme, a low-dissipation and low-dispersion (LD2) scheme was formulated by Löwe et al. [42] and Probst et al. [43], where a higher order extrapolation of the face fluxes is used to control and reduce the numerical dispersion errors. The shock capturing capabilities of the numerical scheme is important, and should not interfere with the scale-resolving properties. In the original formulation by Jameson, a sensor similar to the second derivative of the pressure was formulated to identify shock waves [44]. A different variant of sensor targeting to minimize excessive dissipation in shock/turbulence interaction in LES was formulated by Ducros [45]. The sensor is a slight modification to Jameson’s sensor and involves the local flow vorticity to identify regions with resolved turbulence.

### 1.3 Motivation and Objectives

This thesis has been motivated by the needs of aerodynamic industries, targeting improved simulation accuracy and increased computational efficiency for complex turbulent flows present in aeronautical applications. Although hybrid RANS-LES methods have been developed and implemented over the past two decades, the coherence and joint behavior of numerical schemes, synthetic turbulence injection and modeling techniques remain challenging and interesting research topics that need to pay special attention in order to increase the simulation robustness and accuracy in industrial applications. Additionally, the methodology needs to be able to handle different flow regimes, ranging from subsonic, transonic to supersonic and even hypersonic flows.

The general targets of this thesis is to improve the feasibility of scale-resolving modelling approaches in terms of both computational accuracy and computational efficiency for robust numerical analysis of aerodynamic flows. More specifically, the thesis work has been dedicated to development, implementation and evaluation of the following technical aspects for predicting unsteady aeronautical flows serving industrial applications:

- Robust numerical methods adapted for improved turbulence-resolving capabilities with hybrid RANS-LES methods.
- Synthetic Turbulence Generator (STG) methods adapted in scale-resolving simulations using zonal hybrid RANS-LES methods (including embedded LES) for improved feasibility and for potential industrial use.
- Improved RANS-LES interface methodology with seamless scale- and arbitrary geometry adaptation.

The methodology described above have been implemented into the flow solver M-Edge, which is the CFD package deployed in a set of industries, academia and research institutes (including Saab and FOI in Sweden). It is expected the method developed from the work will be exploited by industries to improve current aircraft designs and meet requirements on future aircraft platforms, and even in academic education for knowledge transfer.

## Chapter 2

# Modeling of Turbulent Flows

This chapter introduces the governing equations for turbulent flows. First, the form of Navier-Stokes equations which are solved for Direct Numerical Simulation (DNS) are presented. These equations need to be filtered in order to reduce the spatial and temporal resolution requirements, to make scale-resolving simulations more accessible to the industry. The filtered Navier-Stokes equations are presented, along with the turbulence modeling methods used in this thesis. A description of the CFD solver used in this thesis then follows, with a detailed outline of the relevant numerical methods used for scale-resolving simulations.

### 2.1 Governing Equations of Fluid Motions

The Navier-Stokes equations for unsteady compressible flow reads

$$\frac{\partial \rho}{\partial t} + \frac{\partial(\rho u_i)}{\partial x_i} = 0 \quad (2.1)$$

$$\frac{\partial(\rho u_i)}{\partial t} + \frac{\partial(\rho u_i u_j)}{\partial x_j} = -\frac{\partial p}{\partial x_i} + \frac{\partial \sigma_{ij}}{\partial x_j} \quad (2.2)$$

$$\frac{\partial(\rho e_0)}{\partial t} + \frac{\partial(\rho e_0 u_j)}{\partial x_j} = -\frac{\partial(p u_j)}{\partial x_j} + \frac{\partial}{\partial x_j} \left[ \kappa \frac{\partial T}{\partial x_j} + u_i \sigma_{ij} \right] \quad (2.3)$$

where the thermal conductivity  $\kappa$  is set to  $\kappa = C_P \mu / P_r$ ,  $C_P$  is the specific heat capacity for constant pressure,  $\mu$  is the molecular viscosity and  $P_r$  is the Prandtl number. The total energy is computed as  $e_0 = e + u_i u_i / 2$ . For a perfect gas we have the internal energy  $e = C_V T$ ,  $C_V = R / (\gamma - 1)$ ,  $\gamma = C_P / C_V$ , where  $C_V$  is the specific heat capacity for constant volume,  $T$  is the temperature,  $R$  is the gas constant and  $\gamma$  is the heat capacity ratio. The equation of state reads

$$p = (\gamma - 1) \left[ \rho e_0 - \frac{1}{2} \rho u_i u_i \right] \quad (2.4)$$

A Newtonian fluid is assumed and the viscous stress tensor is modeled as

$$\sigma_{ij} = \mu \left( \frac{\partial u_i}{\partial x_j} + \frac{\partial u_j}{\partial x_i} - \frac{2}{3} \frac{\partial u_k}{\partial x_k} \delta_{ij} \right) \quad (2.5)$$

To solve this set of equations (2.1)-(2.3) for turbulent flows in DNS, all relevant spatial and temporal scales in the flow field need to be resolved. This means that the grid needs to be fine enough to resolve features on the order of the Kolmogorov length scale

$$\eta = (\nu^3 / \varepsilon)^{\frac{1}{4}} \quad (2.6)$$

where  $\nu$  is the kinematic viscosity and  $\varepsilon$  is the dissipation rate. Likewise, the time step needs to be fine enough to resolve temporal dynamics on the order of the Kolmogorov time scale

$$\tau = (\nu/\varepsilon)^{\frac{1}{2}} \quad (2.7)$$

These resolution requirements for DNS impose a computational cost for industrial flows at high Reynolds numbers which is not feasible today and in the foreseeable future [46]. By filtering the Navier-Stokes equations (2.1) - (2.3), the resolution requirement is reduced. However, this filtering introduces additional unknown terms. Hence, modeling techniques such as, namely, turbulence modeling, are implemented to close the set of equations. The typical filtering process and the filtered Navier-Stokes equations used in this thesis are outlined below.

## 2.2 Modeling Methodologies

The RANS equations are derived by using time-averaging, which can for an arbitrary quantity  $\Phi$  be expressed as

$$\bar{\Phi} = \frac{1}{T} \int_T \Phi dt, \quad \Phi = \bar{\Phi} + \Phi' \quad (2.8)$$

where the instantaneous variable  $\Phi$  is decomposed into a time-averaged part  $\bar{\Phi}$  and a fluctuating part  $\Phi'$ . Note that  $T$  is the time-averaging period in Eq. (2.8) that needs to be sufficiently large.

In LES, a spatial filter is applied instead. This can for a top-hat filter based on the finite volume method be expressed for the quantity  $\Phi$  in 1D as:

$$\bar{\Phi}(x, t) = \frac{1}{\Delta x} \int_{x-0.5\Delta x}^{x+0.5\Delta x} \Phi(\xi, t) d\xi, \quad \Phi = \bar{\Phi} + \Phi' \quad (2.9)$$

Here,  $\bar{\Phi}$  corresponds to a large scale fluctuating part (or resolved part) and  $\Phi'$  corresponds to sub filter scale fluctuating part. In Eq. (2.9), an implicit filter is used through the finite volume discretisation, where the local control volume on the computational grid represents the spatial filter. In addition to the time-averaging in Eq. (2.8) and the spatial filtering in Eq. (2.9), the compressible Navier-Stokes equations contains also Favré filtered [47] quantities. The Favré filter is defined by

$$\tilde{\Phi} = \frac{\bar{\Phi}\bar{\rho}}{\bar{\rho}}, \quad \Phi = \tilde{\Phi} + \Phi'' \quad (2.10)$$

Here,  $(\bar{\cdot})$  means time-averaged quantities when RANS is applied and spatially-averaged quantities when LES is applied. The Favré filtering is denoted by  $(\tilde{\cdot})$ .

After filtering, the compressible Navier-Stokes equations ((2.1) - (2.3)) become

$$\frac{\partial \bar{\rho}}{\partial t} + \frac{\partial(\bar{\rho}\tilde{u}_i)}{\partial x_i} = 0 \quad (2.11)$$

$$\frac{\partial \bar{\rho} \tilde{u}_i}{\partial t} + \frac{\partial (\bar{\rho} \tilde{u}_i \tilde{u}_j)}{\partial x_j} = -\frac{\partial \bar{p}}{\partial x_i} - \frac{\partial \mathcal{T}_{ij}}{\partial x_j} \quad (2.12)$$

$$\frac{\partial (\bar{\rho} \tilde{e}_0)}{\partial t} + \frac{\partial (\bar{\rho} \tilde{e}_0 \tilde{u}_j)}{\partial x_j} = -\frac{\partial (\bar{p} \tilde{u}_j)}{\partial x_j} + \frac{\partial \mathcal{H}_j}{\partial x_j} \quad (2.13)$$

where  $\mathcal{T}_{ij}$  is the total stress tensor  $\mathcal{T}_{ij} \equiv \bar{\rho} \tau_{ij} - \tilde{\sigma}_{ij}$ , and  $\mathcal{H}_j = q_j^t + \kappa \partial \tilde{T} / \partial x_j + \mathcal{T}_{ij} \tilde{u}_j$  are the sum of heat flux plus work done by viscous stresses. The Favré averaged viscous stress tensor is approximated as

$$\tilde{\sigma}_{ij} = \mu \left( \frac{\partial \tilde{u}_i}{\partial x_j} + \frac{\partial \tilde{u}_j}{\partial x_i} - \frac{2}{3} \frac{\partial \tilde{u}_k}{\partial x_k} \delta_{ij} \right) \quad (2.14)$$

The filtered kinetic energy  $k \equiv \tau_{ii}/2$  should be included in the expression for total energy  $\tilde{e}_0 = e + \tilde{u}_i \tilde{u}_i / 2 + k$  due to the filtering process. The equation of state is then given by

$$\bar{p} = (\gamma - 1) \left[ \bar{\rho} \tilde{e}_0 - \bar{\rho} \frac{1}{2} \tilde{u}_k \tilde{u}_k - \bar{\rho} k \right] \quad (2.15)$$

The filtering process has introduced two additional unknowns that need to be modeled, the turbulent stresses and the turbulent heat flux

$$\tau_{ij} = \widetilde{u_i u_j} - \tilde{u}_i \tilde{u}_j \quad (2.16)$$

$$q_j^t = -C_P \bar{\rho} \left( \widetilde{u_j T} - \tilde{T} u_j \right) \quad (2.17)$$

A common approach is to use the Boussinesq approximation, where an eddy viscosity  $\mu_t$  is introduced to relate the turbulent stresses to the mean flow. The assumption is that the turbulent shear stress is proportional to the rate of mean strain rate

$$\tau_{ij} = -\mu_t \left( \frac{\partial \tilde{u}_i}{\partial x_j} + \frac{\partial \tilde{u}_j}{\partial x_i} - \frac{2}{3} \frac{\partial \tilde{u}_k}{\partial x_k} \delta_{ij} \right) + \frac{2}{3} \delta_{ij} \bar{\rho} k \quad (2.18)$$

and the turbulent heat flux is modeled as a diffusion term

$$q_j^t = C_P \frac{\mu_t}{Pr_t} \frac{\partial \tilde{T}}{\partial x_j} \quad (2.19)$$

Obviously, for models based on the Boussinesq assumption, the key has been to find an expression of the eddy viscosity to close the equation system of turbulence flows. Many different models for the turbulent viscosity  $\mu_t$  of varying complexities exists in the literature, in the following sections the turbulence models used in this thesis are outlined.

## 2.2.1 Reynolds-Averaged-Navier-Stokes (RANS)

### The Spalart-Allmaras model

The one-equation model of Spalart and Allmaras (SA) was especially developed for applications of aerodynamic flows and is empirically built as follows [48, 49]:

$$\frac{\partial (\bar{\rho} \tilde{\nu})}{\partial t} + \frac{\partial (\bar{\rho} \tilde{u}_j \tilde{\nu})}{\partial x_j} = C_{b1} \bar{\rho} \tilde{\nu} \tilde{S} + \frac{1}{\sigma} \left[ \frac{\partial}{\partial x_j} \left( (\mu + \bar{\rho} \tilde{\nu}) \frac{\partial \tilde{\nu}}{\partial x_j} \right) + C_{b2} \frac{\partial \tilde{\nu}}{\partial x_j} \frac{\partial \bar{\rho} \tilde{\nu}}{\partial x_j} \right] - C_{w1} \bar{\rho} f_w \left( \frac{\tilde{\nu}}{l_{RANS}} \right)^2 \quad (2.20)$$

where the quantities on the right-hand side correspond to, respectively, production, diffusion, cross diffusion and destruction. The length scale appearing in the destruction term is computed as the distance to the wall  $l_{RANS} = d_w$ . The eddy viscosity is defined as

$$\mu_t = \bar{\rho} \tilde{\nu} f_{\nu 1} \quad (2.21)$$

In order to ensure that  $\tilde{\nu}$  equals  $\kappa y u_\tau$  in the log-layer, buffer layer and viscous sublayer, a damping function  $f_{\nu 1}$  is defined as

$$f_{\nu 1} = \frac{\chi^3}{\chi^3 + c_{v1}^3} \quad \text{with} \quad \chi = \frac{\tilde{\nu}}{\nu} \quad (2.22)$$

The quantity  $\tilde{S}$  in the production term corresponds to a modified vorticity such that it maintains its log-layer behaviour ( $\tilde{S} = \frac{u_\tau}{\kappa y}$ )

$$\tilde{S} = \tilde{\Omega} + \frac{\tilde{\nu}}{\kappa^2 l_{RANS}^2} f_{v2} \quad (2.23)$$

which is accomplished with the function

$$f_{v2} = 1 - \frac{\chi}{1 + \chi f_{v1}} \quad (2.24)$$

In Eq. (2.23) the magnitude of the vorticity tensor is computed as

$$\tilde{\Omega} = \sqrt{2\tilde{\Omega}_{ij}\tilde{\Omega}_{ij}}, \quad \tilde{\Omega}_{ij} = \frac{1}{2} \left( \frac{\partial \tilde{u}_i}{\partial x_j} - \frac{\partial \tilde{u}_j}{\partial x_i} \right) \quad (2.25)$$

In order to obtain a faster decaying behaviour of the destruction term in the outer region of the boundary layer, a function  $f_w$  is utilised

$$f_w(g) = g \left( \frac{1 + c_{w3}^6}{g^6 + c_{w3}^6} \right), \quad g = r + g_{w2}(r^6 + r), \quad r = \frac{\nu}{\tilde{S} \kappa^2 l_{RANS}^2} \quad (2.26)$$

where  $g$  act as a limiter that prevents large values of  $f_w$ . Both  $r$  and  $f_w$  are equal 1 in the log-layer and decrease in the outer region. Constants of the model are

$$\begin{aligned} c_{b1} &= 0.1355, \quad c_{b2} = 0.622, \quad \sigma = 2/3, \quad \kappa = 0.41, \\ c_{w1} &= \frac{c_{b1}}{\kappa^2} + \frac{1 + c_{b2}}{\sigma}, \quad c_{w2} = 0.3, \quad c_{w2} = 2, \quad c_{v1} = 7.1 \end{aligned} \quad (2.27)$$

### The Shear Stress Transport (SST) $k$ - $\omega$ model

The two-equation SST  $k$ - $\omega$  model by Menter [50] was developed for improving predictions of aeronautical flows with strong adverse pressure gradients and separation. The model is a blending of the standard  $k$ - $\varepsilon$  [51] model in the outer part of the boundary layer and the Wilcox  $k$ - $\omega$  model [52] in the near-wall part. The  $k$ - $\varepsilon$  model is transformed into  $k$ - $\omega$

formulation, resulting in a cross diffusion term and modified coefficients, which is then blended with the near-wall  $k - \omega$  via a blending function. The model follows:

$$\begin{aligned}\frac{\partial(\bar{\rho}k)}{\partial t} + \frac{\partial(\bar{\rho}\tilde{u}_j k)}{\partial x_j} &= \frac{\partial}{\partial x_j} \left[ (\mu + \sigma_k \mu_t) \frac{\partial k}{\partial x_j} \right] + P_k - \bar{\rho} \sqrt{k^3} / l_{RANS} \\ \frac{\partial(\bar{\rho}\omega)}{\partial t} + \frac{\partial(\bar{\rho}\tilde{u}_j \omega)}{\partial x_j} &= \frac{\partial}{\partial x_j} \left[ (\mu + \sigma_\omega \mu_t) \frac{\partial \omega}{\partial x_j} \right] + \gamma \frac{\bar{\rho}}{\mu_t} P_k - \beta \bar{\rho} \omega^2 + 2(1 - F_1) \frac{\bar{\rho} \sigma_{\omega 2}}{\omega} \frac{\partial k}{\partial x_j} \frac{\partial \omega}{\partial x_j}\end{aligned}\quad (2.28)$$

The RANS length scale is computed as  $l_{RANS} = \sqrt{k} / (C_\mu \omega)$  with  $C_\mu = 0.09$ . The production term in (2.28) reads as:

$$P_k = \min(\mu_t \tilde{S}^2, 10 \cdot C_\mu \bar{\rho} k \omega) \quad (2.29)$$

Here  $\tilde{S}$  is the magnitude of the strain rate tensor:

$$\tilde{S} = \sqrt{2\tilde{S}_{ij}\tilde{S}_{ij}}, \quad \tilde{S}_{ij} = \frac{1}{2} \left( \frac{\partial \tilde{u}_i}{\partial x_j} + \frac{\partial \tilde{u}_j}{\partial x_i} \right) \quad (2.30)$$

In line with the shear-stress transport idea, the eddy viscosity is formulated

$$\mu_t = \bar{\rho} \frac{a_1 k}{\max(a_1 \omega, \tilde{S} F_2)} \quad (2.31)$$

which complies with  $\overline{u'v'} \leq a_1 k$ , with  $a_1 = 0.31$ . This is in accordance with the Bradshaw assumption, and will reduce the turbulence level around stagnation regions and in adverse pressure gradient boundary layers compared to a standard eddy-viscosity model and the prediction of separated flows is improved. In Eq. (2.28)  $F_1$  and  $F_2$  denote the SST blending functions which read as follows:

$$\begin{aligned}F_1 &= \tanh(\arg_1^4), \quad \arg_1 = \min \left( \max \left[ \frac{\sqrt{k}}{C_\mu \omega d_w}, \frac{500\nu}{d_w^2 \omega} \right], \frac{4\bar{\rho} \sigma_{\omega 2} k}{CD_{k\omega} d_w^2} \right), \\ F_2 &= \tanh(\arg_2^2), \quad \arg_2 = \max \left( \frac{2\sqrt{k}}{C_\mu \omega d_w}, \frac{500\nu}{d_w^2 \omega} \right), \\ CD_{k\omega} &= \max \left( \frac{2\bar{\rho} \sigma_{\omega 2}}{\omega} \frac{\partial k}{\partial x_j} \frac{\partial \omega}{\partial x_j}, 10^{-10} \right)\end{aligned}\quad (2.32)$$

The model constants of the  $k$ - $\varepsilon$  and  $k$ - $\omega$  turbulence models are computed by a blend via  $\gamma = \gamma_1 F_1 + \gamma_2 (1 - F_1)$ :

$$\begin{aligned}\gamma_1 &= 5/9, \quad \beta_1 = 0.075, \quad \sigma_{k1} = 0.85, \quad \sigma_{\omega 1} = 0.5 \\ \gamma_2 &= 0.44, \quad \beta_2 = 0.0828, \quad \sigma_{k2} = 1.0, \quad \sigma_{\omega 2} = 0.856\end{aligned}\quad (2.33)$$

## 2.2.2 Scale-Resolving Modeling

### Large Eddy Simulation

In LES the large scales of turbulent flows are resolved, whereas the scales smaller than the local grid resolution are modeled. A popular and simple expression of computing  $\nu_t$  in Eq. (2.18) is the Smagorinsky model [53]

$$\begin{aligned}\nu_{sgs} &= (C_S \Delta)^2 |\tilde{S}| \\ |\tilde{S}| &\equiv \sqrt{2\tilde{S}_{ij}\tilde{S}_{ij}}\end{aligned}\tag{2.34}$$

where the local filter-width,  $\Delta$ , is taken as the cubic root of local cell volume

$$\Delta = (\delta V_I)^{1/3}\tag{2.35}$$

The model constant  $C_S$  is recognized flow-dependent, taking a values typically in the range of (0.1,0.2). This model implies incorrect scaling close to walls. This is usually alleviated by using a damping function that gives the correct near-wall behaviour. However, the damping functions usually requires the skin-friction velocity in proximity of wall surface as input parameters, possibly leading to complex implementation issues for flow separation where the friction velocity becomes zero.

The Wall-Adapting Local Eddy-Viscosity (WALE) [54] model addresses this issue by providing a more complex expression in terms of resolved spatial derivatives, that automatically fulfills the near-wall scaling. The subgrid viscosity is defined as

$$\begin{aligned}\nu_{sgs} &= (C_m \Delta)^2 \frac{(\mathcal{S}_{ij}^d \mathcal{S}_{ij}^d)^{3/2}}{(\tilde{S}_{ij} \tilde{S}_{ij})^{5/2} + (\mathcal{S}_{ij}^d \mathcal{S}_{ij}^d)^{5/4}} \\ \mathcal{S}_{ij}^d &= \frac{1}{2} \left( \frac{\partial \tilde{u}_i}{\partial x_l} \frac{\partial \tilde{u}_l}{\partial x_j} + \frac{\partial \tilde{u}_j}{\partial x_l} \frac{\partial \tilde{u}_l}{\partial x_i} \right) - \frac{1}{3} \frac{\partial \tilde{u}_m}{\partial x_l} \frac{\partial \tilde{u}_l}{\partial x_m} \delta_{ij}\end{aligned}\tag{2.36}$$

A common value for the model constant for wall bounded flow is  $C_m = 0.325$  [54].

A differential operator based on the singular values of the velocity gradient tensor was proposed in [55] as a basis for an improved SGS eddy-viscosity model. The  $\sigma$ -model was shown to generate zero eddy-viscosity for any two-dimensional or two-component flows, an attractive feature that can unlock Kelvin-Helmholz instabilities and trigger resolved turbulence in free shear layer flows. Similar to the WALE model, it has the proper behavior in near-wall regions. The  $\sigma$ -model reads:

$$\begin{aligned}\nu_{sgs} &= (C_\sigma \Delta)^2 S_\sigma \\ S_\sigma &= \frac{\sigma_3(\sigma_1 - \sigma_2)(\sigma_2 - \sigma_3)}{\sigma_1^2}\end{aligned}\tag{2.37}$$

where  $\sigma_1 \leq \sigma_2 \leq \sigma_3 \leq 0$  are the singular values of the velocity gradient tensor. In quasi two-dimensional flow regions,  $S_\sigma$  is close to zero, which ensures the decrease of the eddy viscosity in shear layers by rapidly reducing the sub-grid viscosity. The constant  $C_\sigma = 1.35$  is chosen according to Nicoud et al. [55].

## Hybrid RANS-LES

A variety of hybrid RANS-LES methods has been developed for the past 25 years. The idea is to exploit the computational efficiency in RANS and the computational accuracy in LES. The hybrid methods produces RANS-type behavior in the vicinity of a solid boundary, where RANS models have successively proven to accurately model attached boundary layers using a moderately coarse mesh. The HRLM switches to LES mode in off-wall regions and in region with separated flow, where LES models have proven to be able to effectively predict unsteady flow features.

Many methods are available in the literature, where the most well-known is the Detached Eddy Simulation (DES) [56, 5, 7, 8] family of models. Two different hybrid methods are used throughout this thesis, the Delayed-DES (DDES) for attached boundary layers where flow separation triggers the generation of resolved turbulence, and the Improved-DDES (IDDES) [8] for boundary layer flows with turbulent inflow content.

### Detached Eddy Simulation (DES)

The DES [56] model modifies the underlying RANS model length scale ( $l_{RANS}$ ) given in Eq. (2.20) for SA and Eq. (2.28) for SST, where  $l_{RANS}$  is replaced by

$$l_{DES} = \min(l_{RANS}, l_{LES}) \quad (2.38)$$

where

$$l_{LES} = C_{DES} \Psi \Delta \quad (2.39)$$

is the LES length scale. Here,  $C_{DES}$  is a modeling constant calibrated in simulations of decaying isotropic turbulence and  $\Psi$  is a correction function to avoid (an unphysical) low Reynolds number damping in the LES region [8]. This correction is not needed for the SST model [57] ( $\Psi = 1$ ), since no low Reynolds number damping functions are present.  $\Delta$  is the local filter width. In the original DES it is defined as

$$\Delta_{max} = \max(\Delta_x, \Delta_y, \Delta_z) \quad (2.40)$$

For an unstructured solver with a dual-grid,  $\Delta_{max}$  in Eq. (2.40) can be ambiguous for cells not aligned with the coordinate directions. In the edge-based solver, such as M-Edge which is used in this work, it is approximated as the maximum edge length of a dual-cell (see Fig. 3.1).

In the near wall region the model reduces to the RANS model, whereas far away from the wall,  $l_{RANS} \gg \Delta$  leading to  $l_{DES} = l_{LES}$  and the model acts as a subgrid scale model. The formulation of the length scale in Eq. (2.38) caused premature switching from RANS to LES, known as grid-induced separation (GIS). The grid-induced separation is caused by the DES model extending the LES region into the boundary layer, where the grid is not fine enough to resolve the turbulent stresses which leads to a reduction of the modeled skin friction and possibly an unphysical flow separation.

### Delayed DES (DDES)

The GIS problem was addressed in the formulation of Delayed DES (DDES) [7], where the DES-length scale in Eq. (2.38) was redefined as

$$l_{DDES} = l_{RANS} - f_d \max(0, l_{RANS} - L_{LES}) \quad (2.41)$$

where  $L_{LES}$  is given in Eq. (2.39) and  $f_d$  is a shielding function

$$f_d = 1 - \tanh([C_1 r_d]^{C_2}) \quad (2.42)$$

which takes on the value unity in the LES region and zero elsewhere. This function aims to prevent LES content from penetrating into the RANS modeled boundary layer. The function  $r_d$  reads

$$r_d = \frac{\nu_t + \nu}{\kappa^2 d_w^2 \sqrt{\frac{1}{2}(\tilde{S}^2 + \tilde{\Omega}^2)}} \quad (2.43)$$

which is similar to  $r$  in Eq. (2.26) for the SA-model and should identify the outer wake of a boundary layer, where the grid is fine enough to resolve the turbulent stresses.

### Improved DDES (IDDES)

For the simulation of wall bounded flows with synthetic turbulence injection in this thesis work, the Improved Delayed DES (IDDES) [8] is employed. The IDDES blends two branches, a DDES-like branch and a WMLES-like branch. The DDES-like branch should become active only when the inflow conditions do not have any turbulent content. The WMLES-like branch is intended to be active only when the inflow conditions used in the simulation are unsteady and impose some turbulent content. An additional criteria on the WMLES-like branch is that the grid is fine enough to resolve boundary-layer dominant eddies. The blending function between the RANS mode and the LES mode reads:

$$l_{IDDES} = \tilde{f}_d(1 + f_e)l_{RANS} + (1 - \tilde{f}_d)l_{LES} \quad (2.44)$$

Here,  $\tilde{f}_d$  is a function that blends between DDES and WMLES, and  $f_e$  is a function to enhance the RANS length scale in the vicinity of the RANS-LES interface in order to reduce the log-layer mismatch. The LES length scale in (2.44) is given by Eq. (2.39) but the the local filter-width  $\Delta$  is replaced by

$$\Delta_{dw} = \min(\max[C_{dw}d_w, C_{dw}\Delta_{max}, \Delta_{wn}], \Delta_{max}) \quad (2.45)$$

The purpose of  $\Delta_{dw}$  in Eq. (2.45) is to give a correct log-layer behaviour in WMLES without the need to alter the value of the modeling constant  $C_{DES}$  adapted to decaying grid turbulence. In Eq. (2.45),  $C_w = 0.15$  and  $\Delta_{wn}$  is the characteristic wall-normal cell size. For an unstructured edge-based solver, this quantity is not defined in a straightforward way. In this thesis, it is approximated by taking the difference between the maximum and the minimum cell face value of the wall distance  $d_w$  for a given cell. The cell face value is computed by the average of the two connecting nodes for a given edge.

## 2.3 Improvements to Modelling

### 2.3.1 LES Length Scale

In the original formulation of the DES model, the the local filter width  $\Delta$  in Eq. (2.39) is set to the maximum cell dimension  $\Delta_{max}$ . It has been shown in several studies that  $\Delta_{max}$  often gives an excess SGS viscosity for flow cases involving free shear layers in LES mode (e.g. [58, 24]). An alternative length scale to alleviate this problem was formulated by Shur et. al [58], where the length scale  $\tilde{\Delta}_\omega$  is based on the local vorticity direction in the flow. For a hexahedral cell  $\tilde{\Delta}_\omega$  is formulated as

$$\tilde{\Delta}_\omega = \frac{1}{\sqrt{3}} \max_{n,m} \|\mathbf{I}_n - \mathbf{I}_m\|, \quad \mathbf{I}_n = \mathbf{n}_\omega \times (\mathbf{r}_n - \mathbf{r}), \quad \mathbf{n}_\omega = \frac{\boldsymbol{\omega}}{\|\boldsymbol{\omega}\|} \quad (2.46)$$

where  $\mathbf{n}_\omega$  is the unit vector aligned with the vorticity vector. This approach adapts the filter width to the local orientation of eddies, thus helping to reduce the problem of delayed transition from RANS to LES in the initial region of the shear layer. The factor  $\frac{1}{\sqrt{3}}$  is needed to recover  $\Delta_{max}$  for cubic cells in isotropic turbulence.

However, as pointed out in [58], replacing  $\Delta_{max}$  with  $\tilde{\Delta}_\omega$  is not enough to fully unlock the Kelvin-Helmholtz instability. To further force the reduction of the turbulent SGS viscosity in free shear layers the  $F_{KH}$  function is added to  $\tilde{\Delta}_\omega$  to give

$$\Delta_{SLA} = \tilde{\Delta}_\omega F_{KH}(\langle VTM \rangle) \quad (2.47)$$

The  $F_{KH}$  function is based on a Vortex Tilting Measure (VTM) with the aim to detect Kelvin-Helmholtz like structures and rapidly reduce the LES filter width. The Vortex Tilting Measure and  $F_{KH}$  are given:

$$VTM = \frac{\sqrt{6} \|(\tilde{\mathbf{S}} \cdot \boldsymbol{\omega}) \times \boldsymbol{\omega}\|}{\boldsymbol{\omega}^2 \sqrt{3tr(\tilde{\mathbf{S}}^2) - [tr(\tilde{\mathbf{S}})]^2}} \max(0.2\nu/\nu_t, 1) \quad (2.48)$$

$$F_{KH} = \max(F_{KH}^{min}, \min[F_{KH}^{max}, F_{KH}^{min} + \frac{F_{KH}^{max} - F_{KH}^{min}}{a_2 - a_1}(\langle VTM \rangle) - a_1]) \quad (2.49)$$

where  $tr(\cdot)$  is the trace operator,  $F_{KH}^{max} = 1.0$  and  $F_{KH}^{min}$ ,  $a_1$  and  $a_2$  are adjustable empirical parameters which are set to 0.1, 0.15 and 0.3 respectively [58]. Local VTM values are averaged over the current and closest neighboring cells, in order to make  $\Delta_{SLA}$  behave as  $\Delta_{max}$  in developed 3D turbulence.  $\langle VTM \rangle$  is close to zero in the quasi-2D regions of the flow, whereas in regions with fully developed turbulence it is of the order of 1.0. The Vortex Tilting Measure  $\langle VTM \rangle$  in in this thesis is computed as a volume average of the neighbouring cells. The function  $F_{KH}$  takes values between zero and one, where one is its natural value and a reduction towards zero takes place in flows where Kelvin-Helmholtz like structures are detected. By achieving this additional reduction of the turbulent SGS viscosity compared to  $\tilde{\Delta}_\omega$ , the two dimensional Kelvin-Helmholtz structures are able to break up and form three dimensional turbulent structures.

### 2.3.2 Zonal Interface Methods

In a zonal approach, a RANS and a LES region is separated by a prescribed interface. A schematic of a zonal approach with the prescribed RANS-LES interface is presented in Fig. 2.1. Here, an upstream region is treated in RANS but further downstream a focusing

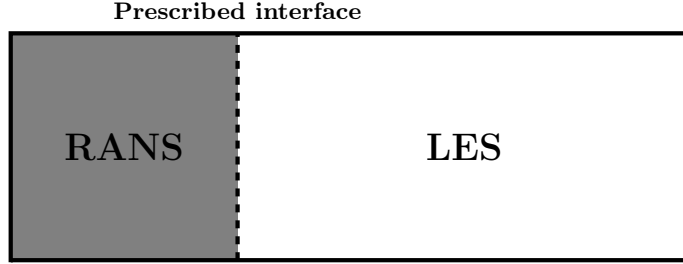


Figure 2.1: *Schematic of RANS and LES regions in zonal hybrid RANS-LES (embedded LES) with wall-normal RANS-LES interface indicated.*

LES region is defined in order to get a better prediction of the flow field. However, if no special care is taken at the prescribed interface, there will be a severe delay in the development of resolved turbulence in the LES region since all turbulent scales are modeled in the RANS region, which is usually called a grey-area transition region. In order to trigger the equations to resolve turbulence and reduce the RANS-to-LES transition region, synthetic turbulent fluctuations can be superimposed onto the RANS mean flow field at the prescribed interface.

### Synthetic Turbulence

The synthetic turbulence methods considered in this theses are the Synthetic-Eddy Method by Jarrin et al. [31] and the Synthetic Turbulence Generator (STG) by Shur et al. [28]. A brief outline of the theory and the implementation of these methods are given in the following sections.

#### Synthetic Eddy Method (SEM)

The velocity fluctuations for the SEM are generated by a fixed number,  $N$ , of artificial eddies and have the representation

$$v'_j(\mathbf{x}, t) = \frac{1}{\sqrt{N}} \sum_{k=1}^N \varepsilon_j^k f_\sigma(\mathbf{x} - \mathbf{x}^k) \quad (2.50)$$

where  $\mathbf{x}^k$  are the locations of the eddies,  $\varepsilon_j^k$  are their respective intensities (with  $\langle \varepsilon_j \rangle = 0$  and  $\langle \varepsilon_j^2 \rangle = 1$ ). The shape function  $f_\sigma(\mathbf{x} - \mathbf{x}^k)$  sets the velocity distribution of the eddy located at  $\mathbf{x}^k$  and is given by

$$f_\sigma(\mathbf{x} - \mathbf{x}^k) = \sqrt{\frac{V_B}{\sigma^3}} f\left(\frac{x - x^k}{\sigma}\right) f\left(\frac{y - y^k}{\sigma}\right) f\left(\frac{z - z^k}{\sigma}\right) \quad (2.51)$$

where  $V_B$  is the volume of the box of eddies explained below,  $\sigma$  is a parameter that controls the size of the vortical structures and  $f$  is a shape function chosen to satisfy the normalization condition

$$\frac{1}{V} \iiint f^2(\mathbf{x}', \sigma) d\mathbf{x}' = 1 \quad (2.52)$$

A function that satisfies this condition is a tent function [31]

$$f(x) = \begin{cases} \sqrt{\frac{3}{2}}(1 - |x|) & \text{if } |x| < 1 \\ 0 & \text{otherwise} \end{cases} \quad (2.53)$$

but is in this study taken as a truncated Gaussian according to

$$f(x) = \begin{cases} \frac{1}{\sqrt{\sqrt{\pi}C \operatorname{erf}(1/C)}} \exp\left(-\frac{1}{2C^2}|x|^2\right) & \text{if } |x| < 1 \\ 0 & \text{otherwise} \end{cases} \quad (2.54)$$

with  $C = 1/3$ . The shape functions for Eqs. (2.53) and (2.54) are shown in Fig. 2.2. The

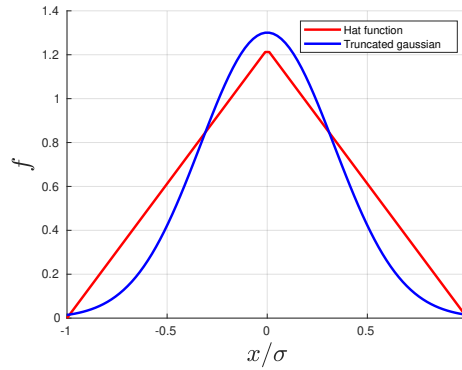


Figure 2.2: *SEM shape functions.*

length scale  $\sigma$  is estimated using information from a RANS model and the maximum local mesh size [31]

$$\sigma = \max[\min(l_{RANS}, \kappa\delta), \Delta_{max}] \quad (2.55)$$

where  $l_{RANS}$  is a RANS length scale and  $\delta$  is the thickness of a boundary layer considered. The virtual eddies are randomly generated in, and convected through, a virtual domain around a given synthetic-forcing region. The virtual domain is given by a box and is generated around the forcing region  $S = \{\mathbf{x}_1, \mathbf{x}_2, \dots, \mathbf{x}_s\}$ , where the minimum and maximum coordinates are defined by

$$x_{i,\min} = \max_{\mathbf{x} \in S} (x_i - \sigma(\mathbf{x})) \quad \text{and} \quad x_{i,\max} = \max_{\mathbf{x} \in S} (x_i + \sigma(\mathbf{x})) \quad (2.56)$$

In order to ensure that the density of eddies inside of the box of eddies is constant and that the synthetic turbulent field is statistically covered by the eddies, the number of

eddies is set as  $N = \max(V_B/\sigma^3)$ . Note the formulation of Eq. (2.56) generates a padding around the forcing domain  $S$  of the maximum eddy size  $\sigma$ . This padding is ignored in the vicinity of a wall or a periodic boundary. If an eddy overlaps a periodic boundary, the eddy position is mirrored to the other side of the periodic boundary in order to impose a periodic fluctuating velocity field. Time correlation of the fluctuating velocity field are imposed by updating the positions of the eddies using the integrated bulk velocity

$$\mathbf{x}^k(t + \Delta t) = \mathbf{x}^k(t) + \mathbf{U}_b \Delta t \quad (2.57)$$

where the integration of  $\mathbf{U}_b$  is carried out over the interface  $S$ . Eddies that leave the box are randomly regenerated at the inlet side of the virtual box, given by the streamwise direction.

### Synthetic Turbulence Generator (STG)

The velocity fluctuations for the STG [28] are computed by superimposing  $N$  Fourier modes:

$$\mathbf{v}'(\mathbf{x}, t) = \sqrt{6} \sum_{n=1}^N \sqrt{q^n} [\boldsymbol{\sigma}^n \cos(k^n \mathbf{d}^n \cdot \mathbf{x}' + \phi^n)] \quad (2.58)$$

where  $n$  denotes the mode number,  $\mathbf{d}^n$  is the random vector that is uniformly distributed over a unit sphere and  $\boldsymbol{\sigma}^n$  is a unit vector normal to  $\mathbf{d}^n$  ( $\boldsymbol{\sigma}^n \cdot \mathbf{d}^n = 0$ ) [26, 29]. These are given by

$$\mathbf{d}^n = \begin{bmatrix} \sin(\Theta^n) \cos(\Phi^n) \\ \sin(\Theta^n) \sin(\Phi^n) \\ \cos(\Theta^n) \end{bmatrix}, \quad \boldsymbol{\sigma}^n = \begin{bmatrix} \cos(\Phi^n) \cos(\Theta^n) \cos(\eta^n) - \sin(\Phi^n) \sin(\eta^n) \\ \sin(\Phi^n) \cos(\Theta^n) \cos(\eta^n) + \cos(\Phi^n) \sin(\eta^n) \\ -\sin(\Theta^n) \cos(\eta^n) \end{bmatrix} \quad (2.59)$$

where  $\Phi^n$ ,  $\Theta^n = \arccos(1 - 2\gamma^n)$  and  $\eta^n$  are random angles with uniform distributions and intervals given in Table 2.1. Here, the uniformly distributed random phase angle  $\phi^n$  in Eq. (2.58) is also shown.

Table 2.1: Intervals for uniformly distributed random variables.

variable	$\Phi^n$	$\gamma^n$	$\eta^n$	$\phi^n$
interval	$[0, 2\pi)$	$[0, 1)$	$[0, 2\pi)$	$[0, 2\pi)$

The normalized mode amplitude  $q^n$  is computed using a modified von Karman spectrum [28] according to

$$q^n = \frac{E(k^n) \Delta k^n}{\sum_{n=1}^N E(k^n) \Delta k^n}, \quad \sum_{n=1}^N q^n = 1 \quad (2.60)$$

where  $k^n$  is the wave number magnitude of the vector  $\mathbf{d}^n$ . Note that the random variables in Table 2.1 is only computed once. A modified position vector  $\mathbf{x}'$  in Eq. (2.58) is introduced to impose time-correlation. Assuming that the streamwise direction is aligned

with the  $x$ -direction, the position vector is expressed as

$$\mathbf{x}' = \begin{bmatrix} \frac{2\pi}{k^n \max(l_e(\mathbf{x}))} (x - U_b t) \\ y \\ x \end{bmatrix} \quad (2.61)$$

The bulk velocity  $U_b$  is integrated over the RANS-LES interface.  $l_e(\mathbf{x})$  corresponds to the length scale of the most energy-containing mode and is given by  $l_e(\mathbf{x}) = \min(2d_w(\mathbf{x}), C_t l_{RANS})$ .  $C_t = 3.0$  is an empirical constant and  $l_{RANS}$  is the local RANS length scale. The set of wave numbers  $k^n$  is fixed and is common for the entire RANS-LES interface. A geometric series is used

$$k^n = k_{\min}(1 + \alpha)^{n+1}, \quad n = 1, 2, \dots, N, \quad \alpha = 0.01 \quad (2.62)$$

to decrease the number of modes compared to a uniform distribution. The number of modes  $N$  in Eq. (2.58) is then obtained by

$$N = \text{ceil} \left( \frac{\ln(k_{\max}/k_{\min})}{\ln(1 + \alpha)} + 1 \right) \quad (2.63)$$

where  $k_{\min} = \pi / \max(l_e(\mathbf{x}))$ , and  $k_{\max} = 1.5 \max(2\pi/l_{\text{cut}}(\mathbf{x}))$ .  $l_{\text{cut}}(\mathbf{x})$  is computed as

$$l_{\text{cut}} = 2 \min(0.3\Delta_{\max} + 0.1d_w(\mathbf{x}), \Delta_{\max}) \quad (2.64)$$

which corresponds to the length scale of the smallest scales that can be resolved by the grid.

### Anisotropic Fluctuations

The velocity fluctuations in Eqs. (2.50) or (2.58) satisfy the restrictions  $\langle v'_i \rangle = 0$  and  $\langle v'_i v'_j \rangle = \delta_{ij}$ , where  $\langle \cdot \rangle$  denotes time averaging. In order to impose the correct Reynolds stress statistics [59] at the interface, the actual fluctuations  $u'_j(\mathbf{x}, t)$  are computed from

$$u'_j(\mathbf{x}, t) = a_{ij} v'_j(\mathbf{r}, t) \quad (2.65)$$

where  $a_{ij}$  is the Cholesky-decomposed Reynolds stress tensor:

$$a_{ij} = \begin{bmatrix} \sqrt{R_{11}} & 0 & 0 \\ R_{21}/a_{11} & \sqrt{R_{22} - a_{21}^2} & 0 \\ R_{31}/a_{11} & (R_{32} - a_{21}a_{31})/a_{22} & \sqrt{R_{33} - a_{31}^2 - a_{32}^2} \end{bmatrix} \quad (2.66)$$

$a_{ij}$  determines the magnitude of the velocity fluctuation as a function of the estimated Reynolds stresses  $R_{ij} = \langle u'_i u'_j \rangle$ , taken as the RANS modeled stresses at the RANS-LES interface.

### Turbulence Injection Methods

The synthetic turbulence methods provide a fluctuating velocity field that is well defined in both space and time. If the LES domain starts directly at the inflow boundary, the fluctuating velocity signal may be imposed as a Dirichlet boundary condition according to

$$\mathbf{u}(\mathbf{x}, t) = \bar{\mathbf{u}}(\mathbf{x}, t) + \mathbf{u}'(\mathbf{x}, t) \quad (2.67)$$

where  $\mathbf{u}(\mathbf{x}, t)$  is the boundary value of the velocity,  $\bar{\mathbf{u}}(\mathbf{x}, t)$  is the mean velocity profile at the boundary and  $\mathbf{u}'(\mathbf{x}, t)$  fluctuating velocity given by Eq. (2.65). However, if the synthetic turbulence is supposed to be injected in an embedded hybrid RANS-LES framework as in Fig. 2.1, where a forcing region is defined to drive the steady RANS velocity to an unsteady resolved turbulent velocity, Equation (2.67) can not be readily applied in a straight forward way.

This problem is addressed in Paper B [60], where suitable source terms are derived and investigated in developing turbulent channel flow and spatially developing boundary layer flow. The source terms are found by performing an expansion of the instantaneous velocity field according to

$$\tilde{u}_i \rightarrow \bar{u}_i + u'_i \quad (2.68)$$

in Eqs. (2.11)-(2.13), where  $\tilde{u}_i$  is the mean flow and  $u'_i$  is an added synthetic part. These source terms are active only in the forcing region, taken as a wall-normal plane in Paper B, that provide a physically consistent way to impose fluctuations at an embedded RANS-LES interface. The interested reader is referred to Paper B for details about the derivation, below we state the results for the corresponding source terms.

### Injection Method 1

Method 1 (M1) represents the injected fluctuations by considering the contribution from the convective flux [61, 22]. The additional source term associated to the fluctuations and stemming from the convective term is

$$\mathbf{Q}_C = S_n \begin{bmatrix} \bar{\rho} V' \\ \bar{\rho}(\tilde{u}_i V' + u'_i(\tilde{V} + V')) \\ \bar{\rho}\tilde{H}V' + \bar{\rho}(\frac{1}{2}(2\tilde{u}_i u'_i + u'_i u'_i))(\tilde{V} + V') \end{bmatrix} \quad (2.69)$$

where  $\tilde{H} = \tilde{E} + \bar{p}/\bar{\rho}$  is the total enthalpy,  $V' = n_i u'_i$ ,  $\tilde{V} = n_i \tilde{u}_i$  and  $u'_i$  is taken from Eq. (2.65). Here,  $S_n$  is the projected cell area in a plane with normal  $n_i$ . The source term in Eq. (2.69) is added to the equations (2.11) - (2.13) to the cells that intersects the prescribed interface.

### Injection Method 2

Method 2 (M2) is a volume source term stemming from the time derivative [62, 63], the contribution reads

$$\mathbf{Q}_T = \frac{\partial(\bar{\rho}u'_i)}{\partial t} \Delta V \quad (2.70)$$

where  $\Delta V$  is the cell volume. In the work by Schmidt et al. [62], they introduced a ratio of the synthetically generated velocity fluctuations  $u'_i$  and the integral time scale  $T$  instead of applying a temporal derivative in order to express the source term. However, this requires knowledge about the integral time scale  $T$ , which may not be readily available. In the work by Probst [63], the term in Eq. (2.70) was discretized using the same time discretization scheme as the underlying flow solver. For a second-order backward difference scheme, this requires the fluctuations at previous times  $u_i'^n$  and  $u_i'^{n-1}$ . It is argued that using the previous fluctuations from the synthetic turbulence generator may decouple the

predicted flow solution from the target synthetic field, and are instead computed as the predicted fluctuations of the flow solver, namely  $u_i^{\prime n} = u_i^n - \langle u_i \rangle$  and  $u_i^{\prime n-1} = u_i^{n-1} - \langle u_i \rangle$ , respectively. This requires time-averaged mean values  $\langle u_i \rangle$ , which are computed as a running-time average. The approach by Probst is adopted in this thesis.

### Injection Method 3

Method 3 (M3) introduces fluctuations by superimposing both previous methods. That is, the contribution from the source terms given by Eq. (2.69) and (2.70) are added to the continuity, momentum and total energy equations, see Eqs. (2.11) - (2.13). By considering the contribution from both the time derivative and convection term, Method 3 should present a more complete formulation than Methods 1 and 2.

### 2.3.3 Improved Seamless Interface Method

The zonal interface method described in Section 2.3.2 is an effective hybrid RANS-LES approach when the prescribed interface can be readily defined, e.g. in flow cases where an attached boundary layer is located upstream of a region with flow separation induced by geometric settings to which the interface can often be referred. A sudden change in the geometry, e.g. a cavity or an obstacle, induces the flow separation and the LES region can easily be identified with prescribed RANS-LES interface beforehand, at which synthetic turbulence can be added if needed. On the other hand, flows where the separation is subjected to adverse pressure gradient [17] or smooth-body separation [64], the location of the interface may become subtle.

A seamless hybrid RANS-LES interface method is investigated in Paper D [65], which requires no a priori knowledge of the RANS-LES interface location that is implicitly incorporated in the modelling formulation. The method aims to express the transfer of kinetic energy from the modeled turbulent scales to the resolved turbulent scales through an energy conservation principle based on the variation of the local hybrid length scale with the intention to accelerate the RANS-to-LES transition.

In regions of variable resolution, the transfer of energy between modeled RANS and resolved LES turbulence is quantified by a commutation residue term, originally formulated by Girimaji and Wallin [21]. They proposed a model for this term related to PANS and indicated extensions to length scale based models such as DES. We seek to exploit and extend this formulation for DES-based models aiming at entailing a more rapid transition between unresolved and resolved turbulent scales in the vicinity of a RANS-LES interface.

The energy balance in the spectral space is illustrated in Fig. 2.3 with  $\kappa_c \propto 1/l_{ref}$  as the spectral cut-off wave number dividing the turbulence energy into the resolved and unresolved parts,  $k_r$  and  $k$ , respectively. For constant resolution, where  $\kappa_c$  is constant in space/time, the energy cascade  $\sigma$  is responsible for the energy exchange between the resolved and unresolved scales. With variable  $l_{ref}$ ,  $\kappa_c$  can vary in time or space and correspondingly the position of the interface between  $k_r$  and  $k$  will change. This leads to an additional mechanism of energy exchange between  $k_r$  and  $k$ . Following Girimaji and Wallin [21], this energy exchange can be described by a commutation residue term,  $P_{Tr}$ ,

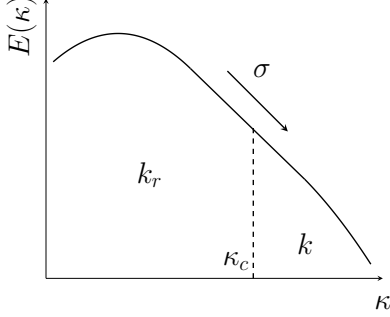


Figure 2.3: *Illustration of energy spectrum with cut-off wave number.*

in terms of the variation of the hybrid length scale  $l_{ref}$ :

$$P_{Tr} = \frac{2}{3} \frac{k}{l_{ref}} \frac{Dl_{ref}}{Dt} \quad (2.71)$$

In the DES concept,  $l_{ref}$  can be taken as any of the DES length scales (e.g.  $l_{DES}$  in Eq. (2.38),  $l_{DDES}$  in Eq. (2.41) or  $l_{IDDES}$  in Eq. (2.44)). The commutation residue term  $P_{Tr}$  in Eq. (2.71) acts as a source/sink term in the equations for  $k$  and  $\omega$ , see Eq. (2.28). In the case of decreasing  $l_{ref}$ , energy is transferred from the unresolved (RANS) to the resolved (LES) scales and  $P_{Tr} < 0$ . Energy conservation dictates that the energy transfer rate,  $P_{Tr}$ , removed from the unresolved scales must be added to the resolved scales. The energy transfer to/from the resolved scales is modelled as a diffusion term in the momentum equation [21]

$$\mu_{Tr} = \frac{\bar{\rho} P_{Tr}}{S^2} \quad (2.72)$$

where  $S = \sqrt{2\tilde{S}_{ij}\tilde{S}_{ij}}$ . It must be emphasized that  $\mu_{Tr}$  and  $\mu_t$  represent different physics and should not be mixed up. For numerical solution they can be added through:

$$\mu_t^* = \mu_t + \mu_{Tr} \quad (2.73)$$

where  $\mu_t^*$  replaces  $\mu_t$  in Eq. (2.18). When resolution improves in space/time, energy is transferred from unresolved to resolved turbulence. This is brought by a negative  $\mu_{Tr}$ . A limit  $\mu_{Tr} \geq -\mu_t$  is introduced to ensure positive total turbulent diffusion.

# Chapter 3

## Numerical Methods for Scale-Resolving Simulations

The CFD solver used in the thesis work is the M-Edge code, which is an edge- and node-based Navier-Stokes flow solver applicable for both structured and unstructured grids [66, 67]. The finite volume discretisation of a node is obtained by applying the integral formulation of the filtered governing equations (2.11)-(2.13) to a control volume surrounding node  $i$ ,

$$\delta V_i \frac{\partial q_i}{\partial t} + \sum_{j=1}^{n_i} F_{ij} \delta S_{ij} + \sum_{j=1}^{n_i} G_{ij} \delta S_{ij} = \delta V_i Q_i \quad (3.1)$$

where  $\delta V_i$  is the control-volume surrounding node  $i$ ,  $q_i = (\rho, \rho u, \rho v, \rho w, \rho E)^T$  are the unknown conservative variables at node  $i$ ,  $F_{ij}$  and  $G_{ij}$  are the cell face convective and viscous fluxes, respectively, between nodes  $i$  and  $j$ ,  $\delta S_{ij}$  is the cell face area connecting the dual control volumes of the nodes, and  $Q_i$  is the source term computed directly at the node. The dual grid control-volumes are computed from a primary grid. A visualisation of the dual and primary grids is shown in Fig. 3.1. The main numerical methods adopted in this thesis are outlined in the following sections.

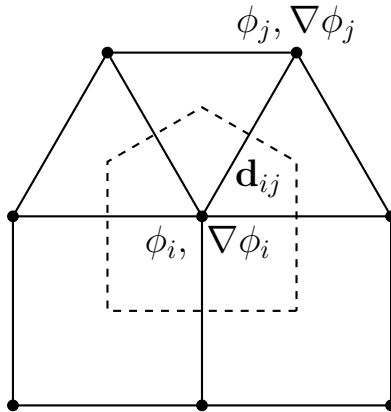


Figure 3.1: Notation for dual grid control-volumes for a finite-volume discretization. The dual grid is generated from a node-centered unstructured grid.

### 3.1 Temporal Discretization

For time-accurate unsteady simulations Eq. (3.1) is integrated in time using a second-order backward difference scheme. A dual-time stepping methodology exploiting an explicit

low-storage multistage Runge-Kutta scheme [44] is used to advance the solution between physical time steps. The convective, diffusive and source terms in Eq. (3.1) are lumped into the residual

$$\delta V \frac{\partial q}{\partial t} + R(q) = 0 \quad (3.2)$$

where the physical time derivative is discretized as

$$\frac{\partial q}{\partial t} = \frac{3q^{n+1} - 4q^n + q^{n-1}}{2\Delta t} \quad (3.3)$$

where  $\Delta t$  is the physical time step. Equation (3.2) is converted to a steady state problem for each physical time step, where a dual-time derivative is introduced

$$\frac{\partial q^*}{\partial \tau} = -R^*(q^*) \quad (3.4)$$

and the residual is modified with the physical time derivative incorporated

$$R^*(q^*) = R(q^*) + \frac{3q^* - 4q^n + q^{n-1}}{2\Delta t} \quad (3.5)$$

The left hand side of Eq. (3.4) is driven to zero at each physical time step and the time accuracy according to Eq. (3.3) is achieved when sufficient convergence is reached. An  $m$ -stage Runge-Kutta scheme is used for time advancement in dual-time

$$\begin{aligned} q^{(0)} &= q^{(k)} \\ q^{(k,m)} &= q^{(0)} - \alpha_m \frac{\Delta \tau}{\delta V} R^*(q^{(k,m-1)}) \\ &\vdots \\ q^{(k+1)} &= q^{(k,m)} \end{aligned} \quad (3.6)$$

where  $\Delta \tau$  is the pseudo-time step and  $\alpha_m$  is the coefficients according to the Runge-Kutta scheme. Convergence is achieved after  $k + 1$  inner-iterations,  $q^{(k+1)} \approx q^{n+1}$ , usually after the residual in Eq. (3.4) has dropped two to three orders of magnitude. A three-stage RK scheme is used to solve the steady-state problem, where the coefficients with good smoothing properties are given by [66]

$$\alpha_1 = \frac{2}{3}, \quad \alpha_2 = \frac{2}{3}, \quad \alpha_3 = 1 \quad (3.7)$$

Note that the order of the dual-time stepping scheme with coefficients chosen as Eq. (3.7) is first-order. However, this does not degrade the solution quality since since the RK scheme, based on the local time step, is adopted to drive the solution converged to a steady state at each physical time step. The convergence of the local time-stepping scheme is further accelerated by using implicit residual smoothing and full-approximation storage (FAS) multigrid [44].

## 3.2 Spatial Discretization

The convective fluxes are discretized according to the second-order central skew-symmetric energy preserving formulation of Kok [68], together with a Jameson-Schmidt-Turkel (JST) artificial matrix dissipation [69, 70]

$$F_{ij} = \tilde{F}_{ij}(q_L, q_R) - D_{ij}(q) \quad (3.8)$$

where  $q_L, q_R$  are extrapolated face values according to a central scheme for reducing dispersion errors [42], the subscripts  $L$  and  $R$  refer to the left and right states at the cell face  $ij$ .  $D_{ij}$  is the JST artificial viscosity term needed for numerical stability, since the central skew-symmetric formulation by Kok does not provide any numerical dissipation to the scheme.

The boundary conditions are implemented in a weak formulation, in which a set of temporary flow variables are computed and used in the calculations of the boundary flux added to the residual. The residual then updates all unknown variables including the boundary values [71]. The viscous fluxes are discretized with a compact second-order central scheme.

### 3.2.1 Numerical Dissipation

The artificial viscosity in Eq. (3.8) is given in the JST scheme [72, 69], which is constructed as a blend of second- and fourth-order artificial dissipation according to

$$D_{ij}(q) = |A|_{ij} \left[ \varepsilon_{ij}^{(2)}(q_i - q_j) - \varepsilon_{ij}^{(4)}(L(q_i) - L(q_j)) \right] \quad (3.9)$$

Here,  $|A|_{ij} = \left| \frac{\partial F}{\partial q} \right|_{ij}$  is the convective flux Jacobian and  $L$  is the undivided Laplacian. In the original "scalar dissipation" formulation of the JST-scheme,  $|A|_{ij}$  is taken as the spectral radius based on the eigenvalues of  $|A|_{ij} = |u| + c$ , where  $u$  and  $c$  are the velocity and the speed of sound, respectively. The terms involving the parameters  $\varepsilon_{ij}^{(2)}$  and  $\varepsilon_{ij}^{(4)}$  correspond to second- and fourth-order dissipation, respectively. The fourth-order dissipation should be active in smooth regions of the flow in order to provide good convergence to a steady state, but should vanish in the vicinity of shock waves as it will produce oscillations. The second-order dissipation term can mitigate oscillations and should be switched on by a sensor that can detect shock waves, as it will lead to degraded accuracy if it is active elsewhere.

The scalar dissipation formulation of  $|A|_{ij}$  provides good convergence properties for steady simulations, usually in steady RANS simulations, but may add too much numerical dissipation and dampen actual physical waves (for example resolved turbulence) in scale-resolving simulations. In this thesis work, a matrix valued artificial dissipation formulation is exploited, where the dissipation for each equation is scaled by the respective eigenvalue of  $|A|_{ij}$ . The convective flux Jacobian in Eq. (3.9) is computed and diagonalized according to Langer [73]:

$$|A|_{ij} = R_{ij} |\Lambda|_{ij} R_{ij}^{-1} \quad (3.10)$$

where  $|\Lambda|_{ij}$  is the diagonal eigenvalue matrix,  $R_{ij}$  and  $R_{ij}^{-1}$  are the left and right eigenvector matrices, respectively, based on the conservative variables. The parameter  $\varepsilon_{ij}^{(4)}$  is taken as the difference between a global constant  $\kappa^{(4)}$  and  $\varepsilon_{ij}^{(2)}$

$$\varepsilon_{ij}^{(4)} = \max[0.0, \kappa^{(4)} - \varepsilon_{ij}^{(2)}] \quad (3.11)$$

such that in presence of shocks the higher differences are switched off in order to prevent oscillations. Typical values of  $\kappa^{(4)}$  in Eq. (3.11) are in the range of 1/32 to 1/64 for RANS applications [73] in order to provide good convergence properties to a steady state solution. However, as shown by Probst et al. [43] and Carlsson et al. [74], these values are not suitable for scale-resolving simulations and will severely dissipate resolved turbulence. LES of decaying grid turbulence and turbulent channel flow indicate that 1/512 to 1/1024 is a suitable range for  $\kappa^{(4)}$  to allow a good trade off between convergence and numerical accuracy in scale-resolving simulations.

The second order dissipation coefficient  $\varepsilon_{ij}^{(2)}$  is chosen as

$$\varepsilon_{ij}^{(2)} = \min[\kappa^{(2)} \max(\Psi_i, \Psi_j), 0.5] \quad (3.12)$$

where  $\kappa^{(2)}$  is a constant and  $\Psi_i$  is a shock-capturing sensor. Note that the choice of  $\varepsilon_{ij}^{(2)} = 1/2$ ,  $\varepsilon_{ij}^{(4)} = 0$  gives a pure first-order upwind scheme in Eq. 3.9, which motivates the limit of 0.5 in Eq. (3.12).

### Shock Capturing Methods

In the presence of shock waves, the flow solver should be able to distinguish discontinuities in the flow field. The standard pressure-based sensor by Jameson [72]

$$\Psi_i = \frac{|\sum_{k=1}^{m_0} (\tilde{p}_i - \tilde{p}_k)|}{\sum_{k=1}^{m_0} (\tilde{p}_i + \tilde{p}_k)} \quad (3.13)$$

identifies regions with large pressure differences, e.g. shock waves, and returns a value close to unity. The numerical scheme is then reduced to a first-order scheme through Eqs. (3.12) and (3.9). This is necessary according to Godunov [75], since any monotonicity preserving numerical scheme in the presence of shock waves can be at most first-order accurate. For regions with a smooth but continuously varying flow field the sensor given by Eq. (3.13) is usually switched off and the scheme follows the fourth-order dissipation in Eq. (3.9).

A different sensor targeted for minimizing excessive dissipation in shock/turbulence interaction in LES was proposed by Ducros [54]. The sensor is a modification to Jameson's sensor and is formulated by multiplying  $\Psi$  of Eq. (3.13) with a local function  $\Phi_i$  defined by

$$\Phi_i = \frac{(\nabla \cdot \mathbf{u})^2}{(\nabla \cdot \mathbf{u})^2 + (\nabla \times \mathbf{u})^2 + \epsilon} \quad (3.14)$$

where  $\epsilon$  is a numerical parameter included to avoid division by zero. The sensor includes the dilation and rotation of the flow field. Thus, regions with resolved turbulence will

reduce the added dissipation. The second-order dissipation is then reformulated as

$$\varepsilon_{ij}^{(2)} = \min[\kappa^{(2)} \max(\Psi_i \Phi_i, \Psi_j \Phi_j), 0.5] \quad (3.15)$$

It was shown to effectively distinguish between shocks and compressible turbulence [54].

### Low-Mach-Number Preconditioning

Low speed preconditioning is often introduced in CFD solvers for compressible flows to reduce the stiffness in the solution procedure for low speed flows with large disparity between the speed of sound and the local velocity. The positive definite preconditioning matrix  $P$  is based on Turkel's preconditioning method [76], where it implemented, for example, for the steady state Equations (3.4)

$$P^{-1} \frac{\partial q^*}{\partial \tau} + R^*(q^*) = 0 \quad \Leftrightarrow \quad \frac{\partial q^*}{\partial \tau} + PR^*(q^*) = 0 \quad (3.16)$$

The preconditioning matrix multiplies the entire residual vector. It is noted that it modifies the speed of sound into an artificial speed of sound close to the local velocity. For time-accurate scale-resolving simulations of low speed flows it is crucial to introduce low speed preconditioning to reduce numerical dissipation, see e.g. [74, 41].

### 3.2.2 Numerical Dispersion

The skew-symmetric energy preserving formulation deploys a particular discretization of the convective terms in the mean flow equations such that good dispersion properties are obtained. The averaged cell face values in the convective numerical flux are formulated as

$$\tilde{F}_{ij} = \begin{bmatrix} (\overline{\rho u})_{ij} \\ (\overline{\rho u \tilde{u}} + \tilde{p} I)_{ij} \\ (\overline{\rho u \tilde{E}} + \tilde{p} u)_{ij} \end{bmatrix} = \begin{bmatrix} \frac{1}{2}(\rho_L u_L + \rho_R u_R) \\ \frac{1}{2}(\rho_L u_L + \rho_R u_R) \frac{1}{2}(u_L + u_R) + \frac{1}{2}(p_L + p_R) I \\ \frac{1}{2}(\rho_L u_L + \rho_R u_R) \left[ \frac{1}{2}(u_L u_R) + \frac{C_L C_R}{\gamma(\gamma-1)} \right] + \frac{1}{2}(u_L p_R + u_R p_L) \end{bmatrix} \quad (3.17)$$

The reader is referred to [42, 68] for the particular choice of averaging ( $\overline{(\cdot)}$ ) and ( $\tilde{(\cdot)}$ ) in Eq. (3.17). For the conventional central flux the subscripts  $L, R$  are given by the nodal values at node  $i$  and  $j$ , respectively. In the low-dispersion scheme by Löwe et al. [42], the left and right face values of the velocity  $u$  and pressure  $p$  are extrapolated from the left and right node values, respectively, by using the gradient of the variable in the nodes, i.e.

$$\begin{aligned} u_L &= u_i + \alpha \nabla u_i \cdot \mathbf{d}_{ij}, & u_R &= u_j - \alpha \nabla u_j \cdot \mathbf{d}_{ij} \\ p_L &= p_i + \alpha \nabla p_i \cdot \mathbf{d}_{ij}, & p_R &= p_j - \alpha \nabla p_j \cdot \mathbf{d}_{ij} \end{aligned} \quad (3.18)$$

where  $\mathbf{d}_{ij}$  is the distance vector between the two nodes. In this thesis work, the gradients are evaluated with a Green-Gauss' approximation, see Eq. (3.20), unless otherwise stated.  $\alpha$  is a parameter that can be chosen to reduce the dispersion error for a specific range of wave numbers. Note that the the speed of sound and density is not extrapolated in the original scheme, since the effects of extrapolation of these quantities are small as reported by Löwe et al. [42]. However, this formulation was only evaluated for subsonic flow cases.

For compressible flow cases involving shock waves, as shown Paper A, it is recommended to extrapolate both density and speed of sound as well

$$\begin{aligned}\rho_L &= \rho_i + \alpha \nabla \rho_i \cdot \mathbf{d}_{ij}, & \rho_R &= \rho_j - \alpha \nabla \rho_j \cdot \mathbf{d}_{ij} \\ c_L &= c_i + \alpha \nabla c_i \cdot \mathbf{d}_{ij}, & c_R &= c_j - \alpha \nabla c_j \cdot \mathbf{d}_{ij}\end{aligned}\quad (3.19)$$

in order to reduce the oscillations in presence of a normal shock, especially for the temperature.

### 3.3 Gradient Reconstruction

Three different gradient reconstruction methods are outlined in this section. The first two are conventional explicit gradient reconstruction methods widely used in CFD codes. The third method is a new implicit gradient reconstruction method developed in Paper C [77]. A summary of these methods is given below.

#### 3.3.1 Explicit Gradient Reconstruction

The divergence theorem (or Green-Gauss) gradient scheme is a popular method for discretizing the gradient operator in second-order accurate finite volume methods. On unstructured grids the discrete version of the divergence theorem is applied to estimate the nodal gradient of a function  $\phi$  at node  $i$  according to

$$\nabla_i \phi \approx \frac{1}{\delta V_i} \sum_{j=1}^{n_i} \phi_{ij} \delta S_{ij} \quad (3.20)$$

where  $\phi_{ij} = \frac{(\phi_i + \phi_j)}{2}$ . The Green-Gauss gradient in Eq. (3.20) is second-order accurate on structured grids but may lose accuracy on skewed and anisotropic unstructured grids.

A more robust method is the least squares based (LSQ) method, which is a technique unrelated to the grid topology. The method relies on a stencil which identifies relevant neighbouring points for use in the gradient reconstruction. A linear system is solved to estimate the coefficients of a polynomial expansion around node  $i$ . Depending on the number of neighbours included to estimate the coefficients of the polynomial expansion, the resulting linear system may become over determined. The nodal gradients can be approximated for an assumed second-order polynomial [78, 79, 80] as

$$\begin{bmatrix} w_{i1} \Delta x_{i1} & w_{i1} \Delta y_{i1} & w_{i1} \Delta x_{i1}^2 & w_{i1} \Delta x_{i1} \Delta y_{i1} & w_{i1} \Delta y_{i1}^2 \\ \vdots & \vdots & \vdots & \vdots & \vdots \\ w_{ij} \Delta x_{ij} & w_{ij} \Delta y_{ij} & w_{ij} \Delta x_{ij}^2 & w_{ij} \Delta x_{ij} \Delta y_{ij} & w_{ij} \Delta y_{ij}^2 \\ \vdots & \vdots & \vdots & \vdots & \vdots \\ w_{iN_b} \Delta x_{iN_b} & w_{iN_b} \Delta y_{iN_b} & w_{iN_b} \Delta x_{iN_b}^2 & w_{iN_b} \Delta x_{iN_b} \Delta y_{iN_b} & w_{iN_b} \Delta y_{iN_b}^2 \end{bmatrix} \begin{bmatrix} \frac{\partial \phi}{\partial x}(\mathbf{x}_i) \\ \frac{\partial \phi}{\partial y}(\mathbf{x}_i) \\ \vdots \end{bmatrix} = \begin{bmatrix} w_{i1}(\phi(\mathbf{x}_i) - \phi(\mathbf{x}_1)) \\ \vdots \\ w_{ij}(\phi(\mathbf{x}_i) - \phi(\mathbf{x}_j)) \\ \vdots \\ w_{iN_b}(\phi(\mathbf{x}_i) - \phi(\mathbf{x}_{N_b})) \end{bmatrix} \quad (3.21)$$

where  $\Delta x_{ij}, \Delta y_{ij}$  are distances between node  $i$  and a neighbouring node  $j$  and are given as

$$\Delta x_{ij} = x_i - x_j, \quad \Delta y_{ij} = y_i - y_j \quad (3.22)$$

The explicit least-squares problem in Eq. (3.21) can be efficiently solved using QR-factorization. In order to improve the condition number of the linear system, the weight in Eq. (3.21) is usually computed using the inverse distance according to

$$w_{ij} = \frac{1}{d_{ij}}, \quad d_{ij} = \sqrt{(x_i - x_j)^2 + (y_i - y_j)^2} \quad (3.23)$$

To increase the order and accuracy of the gradient reconstruction scheme in Eq. (3.21), one can include neighbours to nearest neighbours. However, the compact formulation (by only including nearest neighbours according to Fig. 3.1) is then lost and the implementations on an unstructured grid may become increasingly complicated.

### 3.3.2 Implicit Gradient Reconstruction

In Paper C, a higher-order accurate gradient scheme is formulated to increase the reconstructed gradient accuracy while still maintaining the compact stencil in Fig. 3.1. The coefficients of a higher-order polynomial can be estimated by assuming knowledge of not only the values but also the gradient values of the neighbouring nodes. In numerical analysis this is referred to as Hermite interpolation. The coefficients of the polynomial are estimated by summing over  $j$  nearest neighbours to node  $i$ . This leads to the following set of equations, where the gradient values are implicitly connected:

$$\begin{bmatrix} \Delta x_{i1} & \Delta y_{i1} & \Delta x_{i1}^2 & \Delta x_{i1} \Delta y_{i1} & \Delta y_{i1}^2 & \cdots \\ \vdots & \vdots & \vdots & \vdots & \vdots & \ddots \\ \Delta x_{iN_b} & \Delta y_{iN_b} & \Delta x_{iN_b}^2 & \Delta x_{iN_b} \Delta y_{iN_b} & \Delta y_{iN_b}^2 & \cdots \\ 1 & 0 & 2\Delta x_{i1} & \Delta y_{i1} & 0 & \cdots \\ \vdots & \vdots & \vdots & \vdots & \vdots & \ddots \\ 1 & 0 & 2\Delta x_{iN_b} & \Delta y_{iN_b} & 0 & \cdots \\ 0 & 1 & 0 & \Delta x_{i1} & 2\Delta y_{i1} & \cdots \\ \vdots & \vdots & \vdots & \vdots & \vdots & \ddots \\ 0 & 1 & 0 & \Delta x_{iN_b} & 2\Delta y_{iN_b} & \cdots \end{bmatrix} \begin{bmatrix} L_{i,x} \frac{\partial \phi}{\partial x}(\mathbf{x}_i) \\ L_{i,y} \frac{\partial \phi}{\partial y}(\mathbf{x}_i) \\ \vdots \end{bmatrix} = \begin{bmatrix} \phi(\mathbf{x}_i) - \phi(\mathbf{x}_1) \\ \vdots \\ \phi(\mathbf{x}_i) - \phi(\mathbf{x}_{N_b}) \\ L_{i,x} \frac{\partial \phi}{\partial x}(\mathbf{x}_1) \\ \vdots \\ L_{i,x} \frac{\partial \phi}{\partial x}(\mathbf{x}_{N_b}) \\ L_{i,y} \frac{\partial \phi}{\partial y}(\mathbf{x}_1) \\ \vdots \\ L_{i,y} \frac{\partial \phi}{\partial y}(\mathbf{x}_{N_b}) \end{bmatrix} \quad (3.24)$$

In order to increase the robustness and the condition number of the gradient scheme in Eq. (3.24), normalized distances are introduced according to

$$\Delta x_{ij} = \frac{x_j - x_i}{L_{i,x}}, \quad \Delta y_{ij} = \frac{y_j - y_i}{L_{i,y}} \quad (3.25)$$

The choice of these factors are crucial to avoid growth of the condition number of the reconstruction matrix with grid refinement [81]. Different formulations were investigated in Paper C, the following factors showed robust performance on highly irregular and anisotropic grids with high aspect-ratio:

$$L_{i,x} = \max_j |x_j - x_i|, \quad L_{i,y} = \max_j |y_j - y_i| \quad (3.26)$$

The local system of equations in Eq. (3.24) can effectively be solved using QR-factorization. Coefficients that are connecting gradient values are collected at the left hand side and

summed over the entire grid to form a global system of equations

$$P_{2D} \begin{bmatrix} \frac{\partial \phi}{\partial x} \\ \frac{\partial \phi}{\partial y} \end{bmatrix} = Q_{2D} \begin{bmatrix} \phi \\ \phi \end{bmatrix} \quad (3.27)$$

which has to be solved every solution iteration.

# Chapter 4

## Verification and Validation

This chapter summarizes the selected test cases used for calibration and evaluation of the methods presented in Chapters 2 and 3. In relation to numerical schemes, gradient reconstruction and scale-resolving modelling, the verification and validation conducted are briefly highlighted with computations of relevant test cases. All simulations have been performed with the unstructured compressible flow solver M-Edge, unless otherwise stated.

### 4.1 Verification and Validation of Numerical Schemes

In this section, computations of several test cases are presented for the evaluation of the performance of a proposed low-dispersive and low-dissipative numerical scheme adapted for compressible flows, the LD2C scheme. The scheme has been further verified on the basis of the LD2 scheme proposed by Probst et al. [43] and examined for incompressible flows. The related numerical parameters for both schemes are shown in Table 4.1.

Table 4.1: Numerical parameters for the LD2 scheme and the LD2C scheme adapted further to compressible flows.

Scheme	$\kappa^{(2)}$	$\kappa^{(4)}$	$\alpha_u, \alpha_p$	$\alpha_\rho, \alpha_c$
LD2	0	1/1024	1/3	0
LD2C	5	1/512	1/3	1/3

The value of the shock capturing parameter  $\kappa^{(2)}$  and the extrapolation parameter  $\alpha$  in Eqs. (3.18) and (3.19) in the compressible flow adapted scheme (denoted the LD2C scheme) was established in a shock-tube case in Paper A. The turbulence-resolving properties of the numerical scheme and calibration of the modeling constant  $C_{DES}$  are investigated in simulation of DIT in Section 4.1.1. The turbulence-resolving capabilities of the numerical scheme in wall-bounded flows in subsonic and supersonic conditions are investigated in Section 4.1.2 using IDDES. The LD2C scheme is further evaluated in hybrid RANS-LES of the supersonic baseflow case in Section 4.1.3.

#### 4.1.1 Decaying Isotropic Turbulence

To assess the scale-resolving properties of the numerical scheme for incompressible isotropic turbulence using the LES mode of the SA (Eq. (2.20)) and SST (Eq. (2.28)) turbulence models, the isotropic grid-generated turbulence measured by Comte-Bellot and Corrsin [82] is simulated as a temporal decay on an equidistant isotropic mesh.

The computational domain is a  $2\pi \times 2\pi \times 2\pi$  cube discretized with  $N^3$  equal sized Cartesian control volumes, using three different grid resolutions:  $N = \{32, 64, 128\}$ . The initial velocity distribution with zero mean velocity is obtained from the experimental

energy distribution for  $\tilde{t} = 0$  using an inverse Fourier transformation in a tool provided by Prof. Strelets at St. Petersburg Technical University. The other thermodynamic variables are initiated to uniform fields to simulate an initial turbulent Mach number of  $M_t = 0.1$ .

The turbulence modeling quantities are initialized as follows. The initial eddy viscosity field is computed from the Smagorinsky model (2.34) using the initial fluctuating field. The SA-viscosity  $\tilde{\nu}$  is then computed iteratively using a Newton solver to fulfil  $\nu_t = f_{v1}\tilde{\nu}$ . For the SST-model, the specific dissipation is computed using the Bradshaw [83] assumption:  $\omega = S/\sqrt{C_\mu}$  with  $C_\mu = 0.09$ . The modeled kinetic energy  $k$  is then computed as  $k = \nu_t\omega$ .

Periodic boundary conditions are applied in all directions. The computed results are compared with the experiment by comparing the three dimensional spectrum at times  $\tilde{t} \in \{0.87, 2.0\}$ . The results on three different grids for SA-based and SST-based LES modes are shown in Fig. 4.1 using the LD2C-scheme in Table 4.1. For this case low Mach-number preconditioning is used but the shock capturing constant  $\kappa^{(2)}$  is switched off.

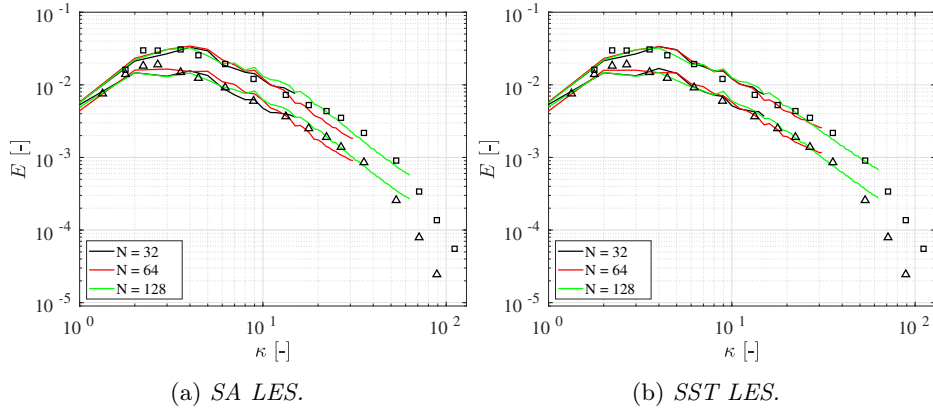


Figure 4.1: *Decaying isotropic turbulence (DIT) using LES mode of hybrid RANS-LES model. Compared with experiments [82] at non-dimensional times  $\tilde{t} = 0.87$  ( $\square$ ) and  $\tilde{t} = 2.0$  ( $\triangle$ ).*

The modeling constant for the SA-based LES model is set to the standard value  $C_{DES} = 0.65$  [7], where the presented spectra in Fig. 4.1a are in good agreement with the experiment. Results for the SST-based LES model is shown in Fig. 4.1b. Here, the model is run in its  $k - \varepsilon$  mode using the standard value  $C_{DES,k-\varepsilon} = 0.61$  [57]. The experimental spectra is well captured on all three grids. The SST model was also run in its  $k - \omega$  mode with  $C_{DES,k-\omega} = 0.78$  (not shown), giving nearly identical results as in Fig. 4.1b. The results shown in Fig. 4.1 indicate that the LD2C scheme can accurately predict the correct decay of isotropic turbulence without the need to recalibrate the standard values of the modeling constant  $C_{DES}$  for the underlying turbulence models.

## 4.1.2 Fully Developed Channel Flow

Fully-developed turbulent channel flow is a useful test case commonly employed for examining the capabilities of resolving turbulence in wall-bounded flows. The test case is employed for the implementation, examination and validation of the numerical scheme and turbulence models using WRLES and the WMLES branch of IDDES. In order to evaluate the methodology for aeronautical applications both subsonic and supersonic conditions and a wide Reynolds number range of the fully-developed turbulent channel flow are simulated.

The computational domain is a rectangular box of height  $2\delta$  ( $y$ ), a length of  $2\pi\delta$  ( $x$ ), and a width of  $\pi\delta$  ( $z$ ), where  $\delta$  is the half-channel height. Periodic boundary conditions are applied in the streamwise and the spanwise directions. To replicate the same wall boundary conditions as the reference DNS [84, 85], no-slip adiabatic conditions are applied in the subsonic cases and no-slip isothermal conditions are applied in the supersonic cases.

To compensate for the lack of a pressure gradient  $\partial p/\partial x$  driving the flow in the streamwise direction, the flow is driven by a forcing term  $f$ , which enforces a specific massflow through the channel in order to achieve a target Reynolds number based on the bulk velocity  $Re_b$ . The target bulk Reynolds number is chosen to satisfy a corresponding Reynolds number based on the friction velocity  $Re_\tau$ , where the target  $Re_\tau$  is derived from DNS results or correlations. Subsonic or supersonic conditions are controlled by specifying the bulk Mach number  $M_b$ . The operating  $Re_b$ ,  $Re_\tau$  and  $M_b$  are defined as in Coleman et al. [86]

$$Re_b = \frac{\bar{\rho}_b \bar{u}_b \delta}{\bar{\mu}_w}, \quad M_b = \frac{\bar{u}_b}{\bar{c}_w}, \quad Re_\tau = \frac{\bar{\rho}_w u_\tau \delta}{\bar{\mu}_w} \quad (4.1)$$

where  $\bar{\mu}_w$  is dynamic viscosity at the wall,  $\bar{c}_w$  is the speed of sound at the wall and  $u_\tau = \sqrt{\tau_w/\bar{\rho}_w}$  is the friction velocity. Details on the computational arrangement of the turbulent channel flow simulations are given in Table 4.2. Wall-resolved (WR) indicates the WALE model given by Eq. (2.36) and wall-modeled (WM) indicates the WMLES branch of IDDES, where both the SA and SST models are considered. WM-Compressible (WMC) indicates that the case is supersonic.

Table 4.2: Summary of channel flow test cases and corresponding grid properties.

Case	$Re_b$	$M_b$	$Re_\tau$	$n_x$	$n_y$	$n_z$	$r$	$\Delta x^+$	$\Delta y^+$	$\Delta z^+$
WR-395	6875	0.15	395	81	97	97	1.1	31	0.37-20	13
WM-395	6875	0.15	395	64	75	64	1.14	40	0.47-38	20
WM-2400	52500	0.15	2400	64	102	64	1.14	239	0.45-219	120
WM-18000	483000	0.15	18000	64	132	64	1.14	1795	0.45-1697	898
WMC-500	7667	1.5	500	64	78	64	1.14	50	0.45-46	25
WMC-1015	17000	1.5	1015	64	90	64	1.14	101	0.47-97	51
WMC-1015F	17000	1.5	1015	128	118	128	1.11	50	0.5-40	25
WMC-5000	100000	1.5	5000	64	112	64	1.14	518	0.5-515	259

## Subsonic Channel Flow

The numerical settings according to the LD2-scheme (using low Mach number preconditioning) in Table 4.1 are evaluated in the nearly incompressible subsonic regime. A random initial velocity field is generated by imposing synthetic fluctuations (STG, see Section 2.3.2) in a  $y - z$  plane in the middle of the channel for one convective time units ( $\text{CTU} = \delta/U_b$ ). The flow is then allowed to develop for two CTU and then averaged over ten CTU. Time averaged quantities are then averaged in the streamwise and spanwise directions.

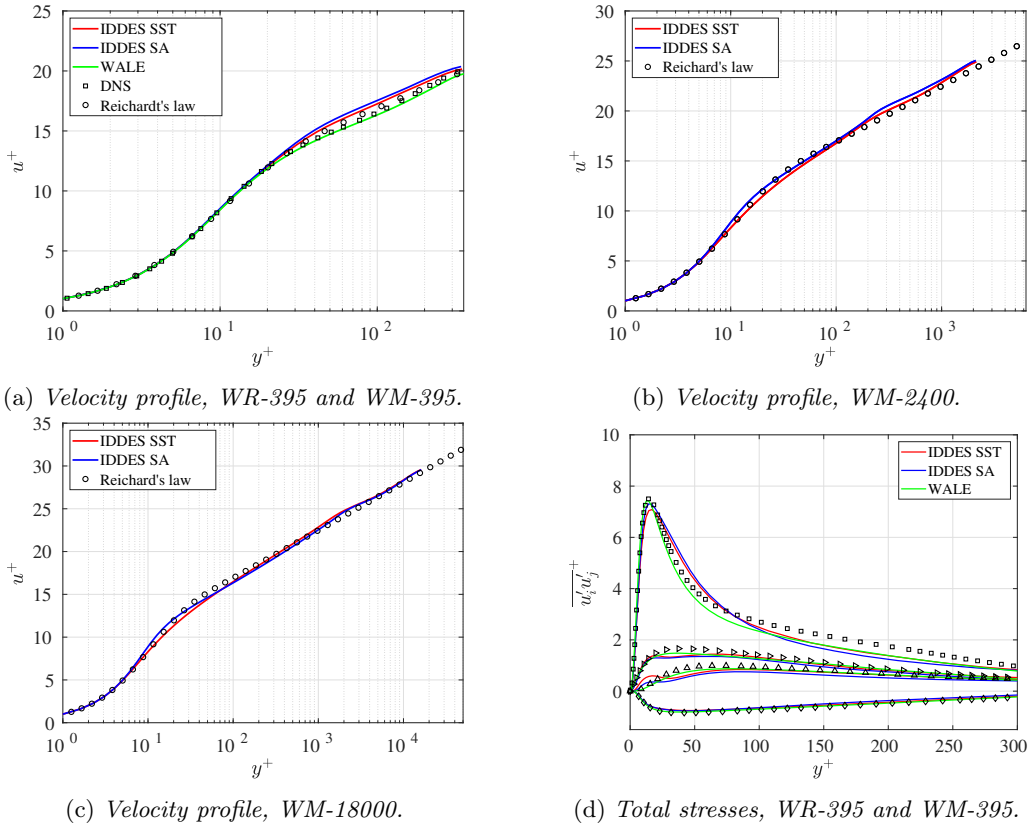


Figure 4.2: Fully developed subsonic channel flow at different  $Re_\tau$  using WRLES and Hybrid RANS-LES IDDES. Turbulence model sensitivity. Results compared with DNS [84] and Reichardt's law [87].  $\square$  :  $\overline{u'u'}$ ,  $\triangle$  :  $\overline{v'v'}$ ,  $\diamond$  :  $\overline{w'w'}$ ,  $\circ$  :  $\overline{u'v'}$  from DNS data [84].

Figure 4.2 presents the mean velocity profile for the subsonic cases at different Reynolds numbers and the total stresses (modeled plus resolved stresses) at  $Re_\tau = 395$ . Excellent agreement with reference DNS [84] for the velocity profile (Fig. 4.2a) and the total stresses (Fig. 4.2d) is achieved using the WALE model at  $Re_\tau = 395$ , where the peak of the streamwise stress  $\overline{u'u'}$  is very well captured. The velocity profile is slightly overpredicted

for the case using IDDES, where the effect is largest for the SA model. The velocity profile for the higher Reynolds number are in general well captured in comparison with the correlation by Reichardt [87], where a small log-layer mismatched can be observed at the RANS-LES interface (at around  $y^+ \approx 200$  for  $Re_\tau = 2400$  as shown in Fig. 4.2b and  $y^+ \approx 2000$  for  $Re_\tau = 18000$  as shown in Fig. 4.2c).

### Supersonic Channel Flow

In the supersonic channel flow simulations the bulk Mach number is set to  $M_b = 1.5$ . No low Mach number preconditioning is used. In this case, both the LD2 and the LD2C schemes are evaluated. The same meshing strategy, initialization of flow field and averaging as in the incompressible cases are used. The Reynolds numbers for cases WMC-500 and WMC-1015 in Table 4.2 are chosen according to the DNS data available by Modesti et al. [85]. The Reynolds number for WMC-5000 was estimated using fully developed RANS to establish the relation between  $Re_b$  and  $Re_\tau$ , since no reference DNS data was found by the author for this combination of higher Reynolds number and Mach number. However, by using proper velocity profile transformation the accuracy of the simulation can be estimated by using incompressible scaling laws.

As discussed by Coleman et al. [86], the so-called Van Driest transformation [88] can be employed for supersonic boundary layers in accounting for mean property variations in compressible turbulent wall-bounded flows. That means that the density weighted velocity profile and Reynolds stresses

$$u_{vD}^+ = \int_0^{u^+} \sqrt{\frac{\bar{\rho}}{\rho_w}} d\tilde{u}^+, \quad \overline{u'_i u'_{jvD}}^+ = \frac{\bar{\rho}}{\rho_w} \overline{u'_i u'_j}^+ \quad (4.2)$$

are expected to follow their incompressible counterparts.

Figure 4.3 presents the mean velocity profile for the cases WMC-500, WMC-1015 and WMC-5000 and the total stresses WMC CMP-1015 using SST-IDDES. Details about the grids used are given in Table 4.2. The results are similar to the subsonic case, the LD2 and LD2C schemes predicts the velocity profile very well in comparison to DNS data for cases WMC-500 and WMC-1015 (Figs. 4.3a and 4.3b), which collapses onto Reichardt's incompressible scaling law. Thus, the good agreement for the LD2 and LD2C schemes with the aforementioned law for the higher Reynolds number in WMC-5000 (Fig. 4.3c) is considered accurate.

However, the Reynolds stresses shown in Fig. 4.4b are not captured as well as in the incompressible case (Fig. 4.2d) for the LD2 and LD2C schemes using the same meshing strategy. For example, the peak value of the streamwise normal stress  $\overline{u' u'_{vD}}^+$  is under predicted in comparison to the DNS result. In order to investigate the grid sensitivity, a finer grid is generated (see WMC-1015F in Table 4.2) with doubled grid resolution in the streamwise and spanwise directions, and a slightly finer resolution in the wall normal direction ( $r = 1.11$ ). As shown in Figs. 4.4a and 4.4b, both the prediction of the velocity profile and the Reynolds stresses are improved.

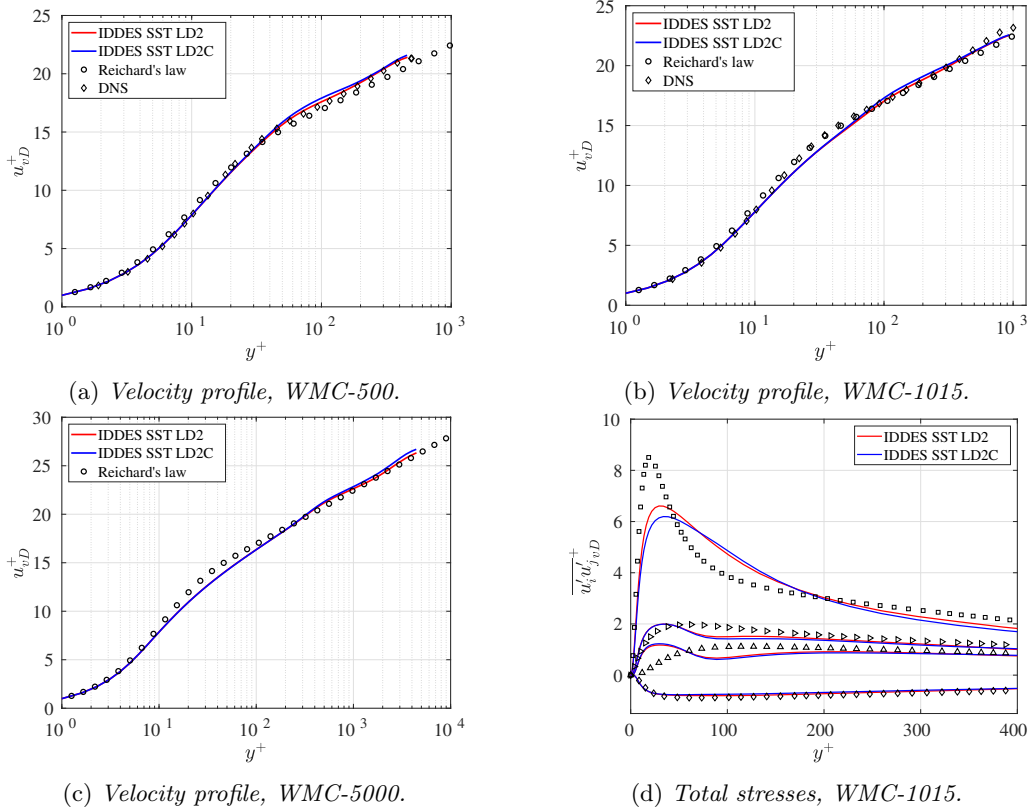


Figure 4.3: Fully developed supersonic channel flow at different  $Re_\tau$  using Hybrid RANS-LES SST-IDDES. Results compared with DNS [85] and Reichardt's law [87].  $\square$  :  $\overline{u' u'}_{vD}$ ,  $\triangle$  :  $\overline{v' v'}_{vD}$ ,  $\triangleright$  :  $\overline{w' w'}_{vD}$ ,  $\diamond$  :  $\overline{u' v'}_{vD}$  from DNS data [85].

### 4.1.3 Supersonic Baseflow

A supersonic flow downstream of a blunt-based cylinder is characterized by expansion waves triggered by the sharp turn of the flow over the base corner. A separation bubble with a low pressure recirculation region contained by a shear layer is formed behind the base. The shear layer undergoes recompression and reattaches at the downstream end of the separation bubble along the symmetry axis. Due to the recompression, a shock wave is formed. A visualisation of the computational domain and the flow field is shown in Fig. 4.5. This kind of flow is commonly found behind high-speed projectiles, and the low pressure region behind the base can cause drag which can be a major part of the total drag. Thus, the modelling needs to be able to accurately predict the base pressure, along with other relevant properties such as the size of the recirculation bubble and turbulent properties subject to strong compressibility effects. For this flow, experimental data are available from the study by Herrin and Dutton [89]. This test case was chosen to evaluate the LD2C scheme in a flow with strong turbulence/shock-wave interaction.

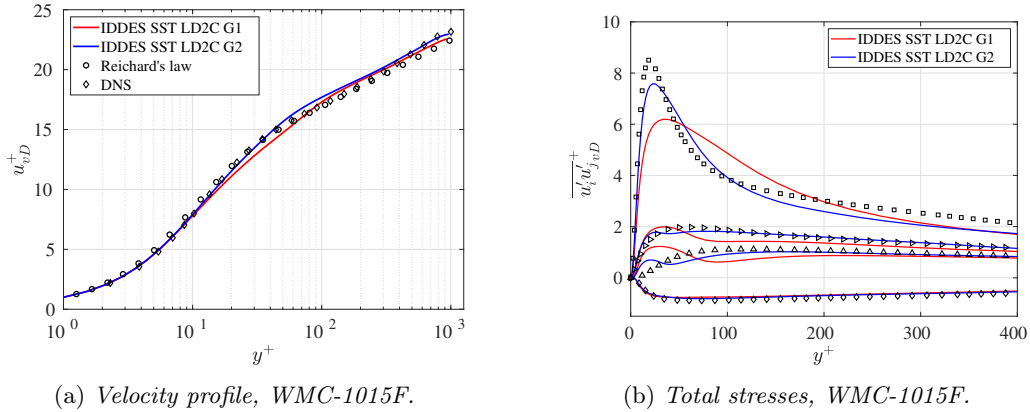


Figure 4.4: Fully developed supersonic channel flow for cases WMC-1015 (G1) WMC-1015F (G2) using Hybrid RANS-LES SST-IDDES. Results compared with DNS [85] and Reichardt's law [87].  $\square$  :  $\overline{u'u'}_{vD}^+$ ,  $\triangle$  :  $\overline{v'v'}_{vD}^+$ ,  $\triangleright$  :  $\overline{w'w'}_{vD}^+$ ,  $\diamond$  :  $\overline{u'v'}_{vD}^+$  from DNS data [85].

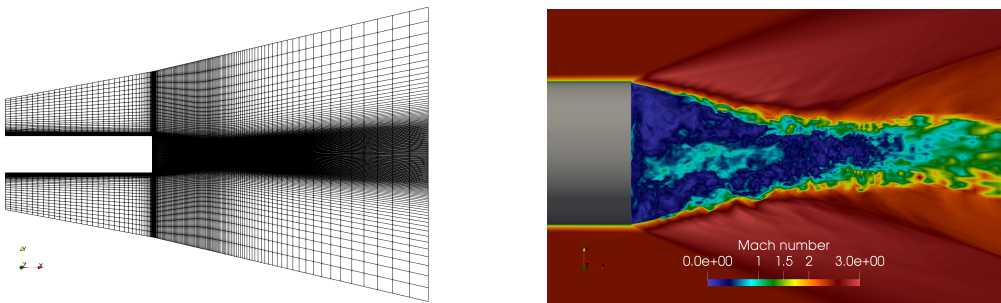


Figure 4.5: Supersonic base flow. Illustration of computational domain (left) and visualization of flow field in the near wake of the cylinder (right). Simulation results acquired using LD2C on the finest grid.

Table 4.3: Summary of supersonic base flow grid properties.  $N_\theta$  indicates number of cells used in the azimuthal direction.

Grid	$N_{cells}$	$N_\theta$	Type
G1	$1.82 \cdot 10^6$	128	Baseline
G2	$2.06 \cdot 10^6$	96	Refined shear layer
G3	$8.51 \cdot 10^6$	176	Refined shear layer/wake region

The flow includes a trailing wake of a circular cylinder with adiabatic walls aligned with a uniform supersonic flow, with a free stream Mach number of  $M_\infty = 2.46$ . The Reynolds number based on the free stream velocity  $U_\infty$ , base radius  $R$  and free stream viscosity  $\nu$  is set to  $Re_R = 1.632 \cdot 10^6$ . Three different grids are considered. A baseline grid with

$N_{cells} = 1.82 \times 10^6$  cells (G1) is used, which was designed by FOI in the DESider project [90]. Two new grids were generated<sup>1</sup>, a grid with improved resolution in the shear layer consisting of  $N_{cells} = 2.06 \times 10^6$  cells (G2), which was designed to match the resolution used in Guseva et al. [91]. The third grid considered contains  $N_{cells} = 8.51 \times 10^6$  cells (G3), where several cells in the axial and radial directions have also been added in the recirculation region downstream the base.

The simulations are performed using the SA-DDES, where the length scale  $\Delta = \Delta_{SLA}$  (see Eqs. (2.39) and (2.41)) is chosen in order to trigger an early development of resolved fluctuation in the separated shear layer. A time step of  $\Delta t = 0.018R/U_\infty$  is used in the computation. After 10000 time steps, the flow is averaged for 20000 time steps. However, it is observed that the mean flow is still slightly asymmetric after time averaging, which is diminished by further averaging the solution in the azimuthal direction.

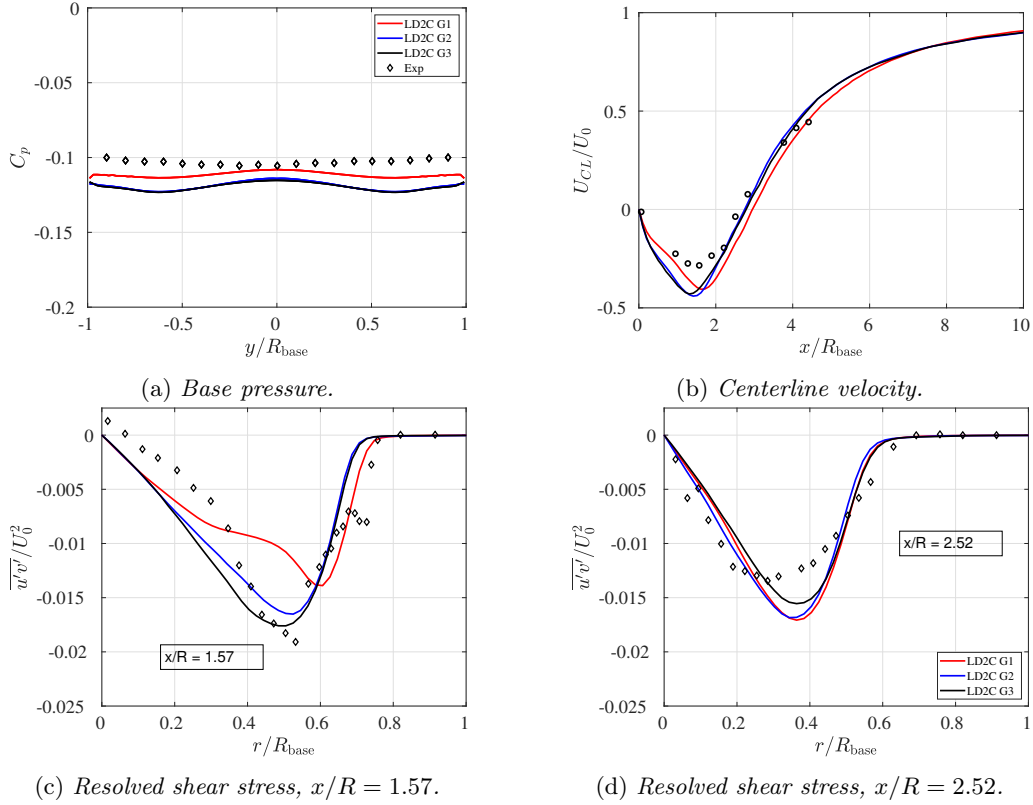


Figure 4.6: Supersonic base flow using Hybrid RANS-LES SA-DDES. Results compared with experiment [89].

Time- and azimuth-averaged flow properties are shown in Fig. 4.6. The base pressure

<sup>1</sup>The grids G2 and G3 were generated using G3D::Mesh with the help of fellow PhD-student Gonzalo Montero Villar. The help is much appreciated.

is presented in Fig. 4.6a, where the experimental results yield a relatively flat profile around  $C_p = -0.102$ . The simulations show radial variations along the base and in general an under predicted base pressure coefficient. However, a wavy base pressure profile and in general lower base pressure values are also observed in the works of Simone et al. [92] and Guseva et al. [91].

The previous trends can be explained by investigating the behavior of the centerline streamwise velocity component in Fig 4.6b. The simulations predicts the reattachment point fairly well ( $x/R \approx 2.9$  on G1  $x/R \approx 2.7$  on G2 and G3) as compared to the experimental value  $x/R = 2.67$ . On the other hand, the reverse flow inside the recirculation region is in general over predicted, which gives rise to the under predicted base pressure levels in Fig. 4.6a. Figures 4.6c and 4.6d present a comparison of the predicted and measured fields of turbulent shear stresses at locations  $x/R = 1.57$  and  $x/R = 2.52$  downstream of the cylinder base, respectively. The shear stress magnitude is slightly under predicted on the coarsest grid G1 at  $x/R = 1.57$  but is in very good agreement on the finer grids G2 and G3.

## 4.2 Verification of Gradient Reconstruction

A new method for gradient reconstruction is presented in Paper C. In order to assess the order of accuracy and robustness of the least-squares gradient reconstruction methods given in Section 3.3, the numerical gradient of a known smooth test function is compared to its analytical value on consecutively refined meshes [93, 94]. The function is evaluated for each interior node through several refinement levels for a set of different unstructured, isotropic and high-aspect-ratio grids. The  $L_1$  and  $L_2$  errors in the resulting numerical gradient are calculated as

$$L_1 = \frac{\sum_i^N |\nabla\phi_{i,num} - \nabla\phi_{i,ana}|}{N}, \quad L_2 = \left( \frac{\sum_i^N |\nabla\phi_{i,num} - \nabla\phi_{i,ana}|^2}{N} \right)^{1/2} \quad (4.3)$$

where  $N$  is the number of nodes,  $\nabla\phi_{i,num}$  and  $\nabla\phi_{i,ana}$  are the numerical and analytical gradients, respectively. The reconstruction schemes are implemented in a stand alone MATLAB script.

The implicit least squares (ILSQ) scheme detailed in Section 3.3.2 is evaluated assuming a fourth-order polynomial order. Since the accuracy of interior nodes is the scope in this thesis, it is assumed that the gradient values at the boundary are known. The compact implicit gradient scheme is compared to the standard distance weighted explicit LSQ (ELSQ) gradient reconstruction scheme given by Eq. (3.21). We consider only connecting neighbours in the LSQ formulation according to Fig. 3.1. This limits the ELSQ schemes to maximum second-order schemes. The test function for the first case is given by:

$$f(x, y) = \sin(\pi x) \sin(\pi y) \quad (4.4)$$

The function in Eq. (4.4) is evaluated on a rectangular domain given by  $[0, 1] \times [0, 1]$  shown in Fig. 4.7a and is discretized using mixed elements (quadrilaterals and triangles). Note that vertices of the elements are randomly perturbed in order to fully remove any

structure in the grid. This is done in order to remove any favorable cancellation of higher-order error terms.

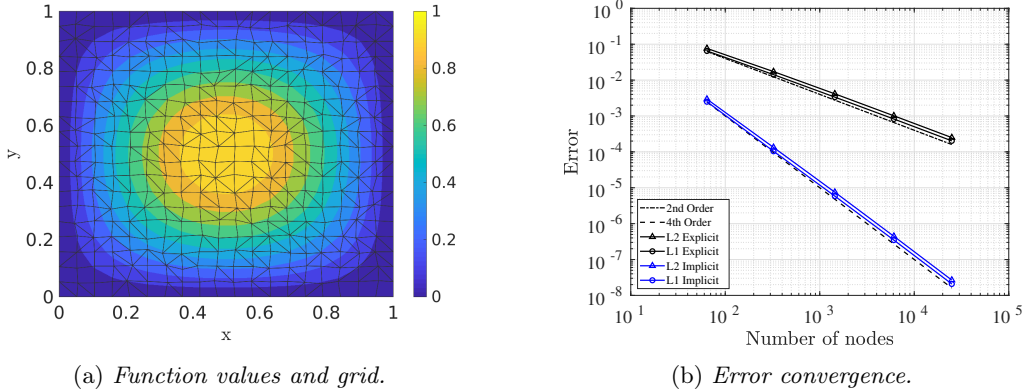


Figure 4.7: Gradient reconstruction of an analytical function. Mixed elements on isotropic domain size.

The order of convergence of the error is shown in Fig. 4.7b. The ILSQ scheme yields a robust fourth-order accuracy in the L1 and L2 error norms using a compact stencil, and indicates that the ILSQ gradient reconstruction formulation is insensitive to grids with mixed quadrilaterals and triangles. The ELSQ scheme attains its prescribed second-order scaling using the same compact stencil. In order to evaluate the performance of the gradient reconstruction methods on highly stretched grids, a different problem is considered. The test function is given by:

$$f(x, y) = \sin(\pi x) \sin(4000\pi y) \quad (4.5)$$

Equation (4.5) is evaluated on a rectangular domain given by  $[0, 1] \times [0, 0.0005]$ . Using this domain size, elements with aspect-ratio of 2000 is considered. This setup models a typical boundary layer problem [94], where the solution variation is predominant in the direction of small grid spacing and an anisotropic grid is specifically tailored to represent the solution anisotropy. The computational domain and the test function are presented in Fig. 4.8. The same mixed element discretization is used as in the previous case.

The order of convergence of the L1 and L2 error norms are shown in Fig. 4.8b. Both methods yield the prescribed accuracy, the ILSQ shows fourth-order convergence and the ELSQ scheme shows second-order convergence. Note that the error levels are higher compared to the case with the isotropic domain size in Fig. 4.7. This is due to the resulting error of the gradient in the direction of the anisotropic scaling being much higher than in the other direction with no stretching. Nevertheless, the ILSQ scheme shows the correct fourth-order scaling on both test cases and are several orders of magnitude more accurate than the standard ELSQ scheme. For example, to reach a similar order of error, the standard ELSQ scheme need to use a discretization of approximately  $2.5 \cdot 10^4$  nodes compared to  $3.0 \cdot 10^2$  nodes used by the ILSQ scheme.

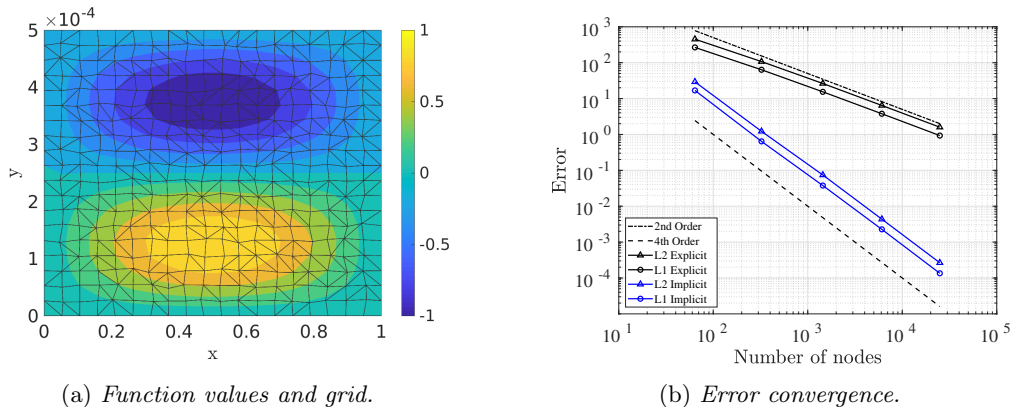


Figure 4.8: Gradient reconstruction of an analytical function. Mixed elements on highly anisotropic domain size. Aspect ratio  $AR = 2000$ .

### 4.3 Examination of Turbulence Injection Methods

This section evaluates the performance of the zonal hybrid RANS-LES approach outlined in Section 2.3.2. The purpose of this section is to assess the injection methods (M1-M3) used in combination with the SEM and STG synthetic turbulence methods. The zonal methodology is evaluated in a hybrid RANS-LES of the spatially developing zero-pressure-gradient (ZPG) turbulent boundary layer. This test case was evaluated in Paper B, where the developing turbulent channel flow at  $Re_\tau = 5200$  was also evaluated.

#### 4.3.1 Spatially Developing Boundary Layer Flow

Simulations of spatially developing boundary layers are essential in the aeronautical industry in order to achieve accurate predictions of aircraft drag. The spatially developing zero-pressure-gradient (ZPG) turbulent boundary layer over a smooth flat plate is therefore simulated using the SA-IDDES with a prescribed wall-normal RANS-LES interface (see Fig. 2.1) located inside the boundary layer. A RANS region is prescribed by forcing  $l_{IDDES} = l_{RANS}$  in Eq. (2.44) between  $0 \leq x/\delta_0 \leq 4$ , and an embedded interface is prescribed at  $x/\delta_0 = 4$ , where  $\delta_0$  is the initial boundary layer thickness. Downstream of this interface, the IDDES length scale in Eq. (2.44) is unmodified. Synthetic turbulent fluctuations and an eddy viscosity treatment for the SA-model described in Paper B are imposed at the embedded interface in order to obtain a rapid development of downstream turbulence-resolving LES flow.

The Reynolds number range covered by the simulation is approximately  $3000 \leq Re_\theta \leq 6000$ , where  $\theta$  is the momentum thickness computed according to

$$Re_\theta = \frac{U_0 \theta}{\nu}, \quad \theta = \int_0^\delta \frac{u}{U_0} \left(1 - \frac{u}{U_0}\right) dy \quad (4.6)$$

where  $U_0$  is the free stream velocity and  $\nu$  is the dynamic viscosity. The Mach number

based on the free stream velocity is  $M_0 = 0.2$ . Profiles of  $u$ ,  $v$  and  $\nu_t$  from a precursor RANS simulation using the SA model are prescribed at the inlet boundary. Adiabatic conditions are applied at the bottom wall boundary and characteristic Riemann boundary conditions is applied at the top and outlet boundaries. Periodic boundary conditions are applied in the spanwise direction.

The grid used for the simulation is designed by Onera and used in the EU-FP7 Go4Hybrid [95], the Garteur AG54 projects and in Deck et al. [96]. The dimensions of the computational domain in the streamwise, spanwise and in the wall-normal directions are, respectively,  $L_x = 113\delta_0$ ,  $L_z = 5\delta_0$  and  $L_y = 52\delta_0$ . Note that for  $x/\delta_0 > 77$ , grid cells are stretched in the streamwise direction in order to progressively damp the turbulent fluctuations. This procedure is common to ensure that the domain of interest is free from wave reflections from the outlet. Details about the grid used are given in Table 4.4.

Table 4.4: Grid parameters of the ZPG turbulent boundary layer.  $Re_{\theta_0}$  and  $Re_{\tau_0}$  are computed with the initial boundary layer thickness  $\delta_0$ .

$Re_{\theta_0}$	$Re_{\tau_0}$	$M_\infty$	$n_x$	$n_y$	$n_z$	$\Delta x^+$	$\Delta y_{min}^+$	$\Delta z^+$
3030	1065	0.2	587	127	103	100-200	2	50

The injection methods M1-M3 (see Section 2.3.2) are assessed by imposing synthetic fluctuations from either the STG given by Eq. (2.58) or the SEM given by Eq. (2.50) at the wall-normal RANS-LES interface. The fluctuations are scaled with the Cholesky tensor given by Eq. (2.66), where the Reynolds stress tensor is taken as the RANS stresses from a precursor RANS simulation.

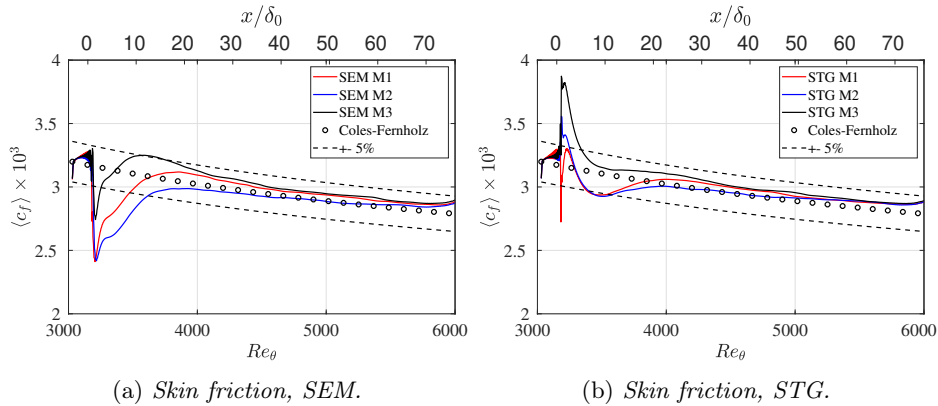


Figure 4.9: *Developing turbulent boundary layer at  $Re_\theta = 3030$  using Hybrid RANS-LES SA-IDDES. Synthetic turbulence model and turbulence injection method sensitivity. Results compared with Coles-Fernholz correlation [97]. Prescribed wall-normal RANS-LES interface is located at  $\tilde{x}/\delta_0 = 0$ .*

Figure 4.9 shows the resulting skin friction coefficient in comparison with the Coles-Fernholz correlation [97]. It can be concluded that the proposed method M3, which is

the combination of M1 and M2, performs best for both the SEM and STG. The initial sudden decrease of the skin friction coefficient is characteristic for the SEM, but this effect seems to be mitigated by using method M3. On the other hand, the initial skin friction is over predicted for the STG in combination with M3, but the correct asymptotic behavior is reached quicker compared to M1 and M2. The correct trend of M3 is reached after roughly  $5\delta_0$  when using either the SEM or the STG, a clear improvement compared to M1 and M2. However, it is important to highlight that all simulations are within a 5% margin after  $10\delta_0$  from the reference correlation, and give a correct decay of the skin friction further downstream in the boundary layer, as shown in Fig. 4.9.

The difference between the methods with respect to the mean velocity profile and resolved stresses measured at  $Re_\theta = 4060$  are very small and yield similar small deviation from DNS [98], as shown in Figs. 4.10a and 4.10b. Here, only the results are shown for the STG, the results for the SEM are very similar.

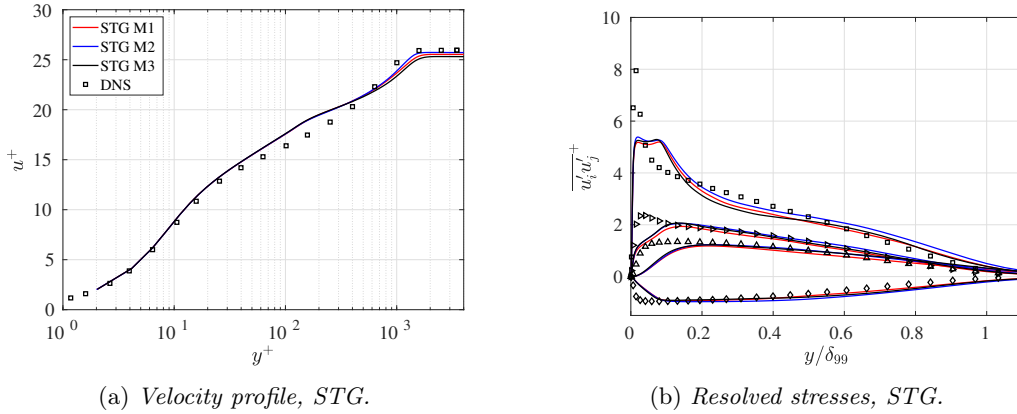


Figure 4.10: *Developing turbulent boundary layer using Hybrid RANS-LES SA-IDDES. Synthetic turbulence model and turbulence injection method sensitivity. Profiles are measured at at  $Re_\theta = 4060$  and compared with DNS data [98]:  $\square$  :  $\overline{u'u'^+}$ ,  $\triangle$  :  $\overline{v'v'^+}$ ,  $\triangleright$  :  $\overline{w'w'^+}$ ,  $\diamond$  :  $\overline{u'v'^+}$ .*

## 4.4 Verification of Seamless GAM Methodology

This section reports results from Paper D, which evaluate the proposed seamless Grey-Area Mitigation (GAM) methodology outlined in Section 2.3.3. The seamless methodology is evaluated for a mixing shear layer flow case using hybrid RANS-LES. Additional results of flow over a wall-mounted hump (Hump flow) is presented in Paper D. A baseline formulation is considered, the  $k - \omega$  SST DDES model (Eqs.(2.28) and (2.41)) using the filter width  $\Delta = \tilde{\Delta}_\omega$ . The length scale based commutation term (CT) is implemented as a source term in the  $k$  and  $\omega$  equations through Eq. (2.71). The contribution to the resolved Eqs.(2.11) - (2.13) is implemented as a modified eddy viscosity  $\mu_t^*$  (see Eq. (2.73)), which replaces  $\mu_t$  in Eq. (2.18). In addition to the length scale based commutation term, the

$\sigma$ -DDES model by Mocket et al. [99] is evaluated in combination with the commutation term or as a stand-alone GAM methodology.

#### 4.4.1 Mixing Shear Layer Flow

Mixing layer flows and free shear flows are often encountered in aeronautical applications, for example jet flows and flows downstream of aircraft wings after the trailing edge. The free shear layer flow evaluated in this Section was investigated experimentally by Delville [100]. The computational domain includes a very thin flat plate, with turbulent boundary layers on each side. A mixing layer is formed in the region downstream of the flat plate trailing edge. The experimental boundary layer properties at the trailing edge are presented in Table 4.5.

Table 4.5: Flow parameters of mixing-layer case. Data from experiment [100].

Measure	Notation	High vel. BL	Low vel. BL
Velocity	$U_\infty$	41.54 m/s	22.40 m/s
Thickness	$\delta$	9.6 mm	6.3 mm
Displ. thick.	$\delta_1$	1.4 mm	1.0 mm
Mom. thick.	$\theta$	1.0 mm	0.73 mm
Shape factor	$H$	1.35	1.37
Re based on $\theta$	$Re_\theta$	2900	1200
Turbulence level	$u'/U_\infty$	$\sim 0.3\%$	$\sim 0.3\%$

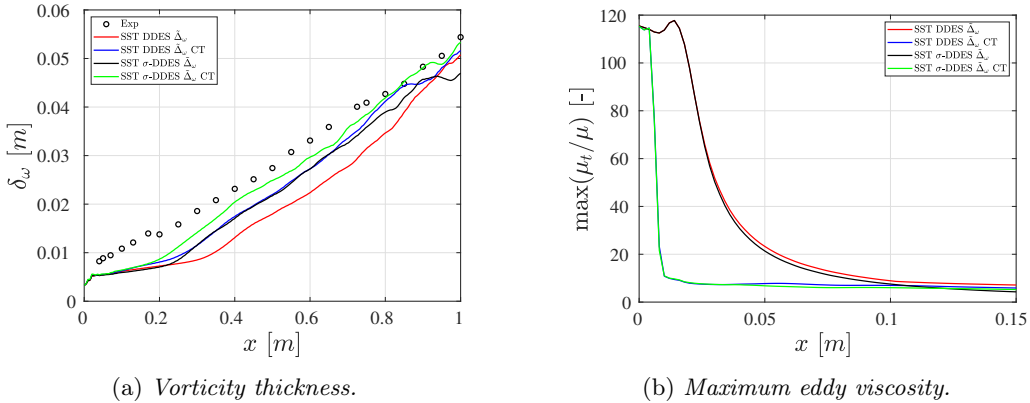


Figure 4.11: *Mixing shear layer flow using Hybrid RANS-LES SST-DDES. Commutation term is indicated by CT. Results compared with experiment [100].*

The focus region, i.e. the region from the flat plate trailing edge at  $x = 0$  to  $x = 1$  m, is meshed with  $(n_x, n_y, n_z) = (640, 196, 96)$  cells. The grid is equidistant in the streamwise  $x$ -direction and spanwise  $z$ -direction,  $\Delta x = \Delta z = 1.5625$  mm. The total number of hexahedral grid cells are 13.7 million. A timestep of  $\Delta t = 2.5 \times 10^{-5}$  seconds is used. The upstream boundary layers are treated in RANS mode and the DDES model automatically

switches to LES after the trailing edge. The growth of the mixing layer, the vorticity thickness, computed as

$$\delta_\omega = \frac{U_a - U_b}{(\partial U / \partial y)_{y=0}} \quad (4.7)$$

is presented in Fig. 4.11a. The baseline case clearly underpredicts the growth of the shear layer. By applying the the commutation term, the  $\sigma$ -DDES model or a combination of those gives improved results, where the agreement with the experimental result is significantly improved for after  $x > 0.2$  m. The maximum eddy viscosity at the initial part of the shear layer is shown in Fig. 4.11b. The effect of the commutation term is large, where the eddy viscosity is rapidly reduced. Without the commutation term, such a reduction is relatively slow. The lower eddy viscosity levels contributes to a rapid growth of resolved turbulence, which is visualised in Fig. 4.12. As shown, the resolved shear stress is better predicted at station  $x = 0.2$  m, where the prediction incorporating both the commutation terms combined with  $\sigma$ -DDES gives the best result.

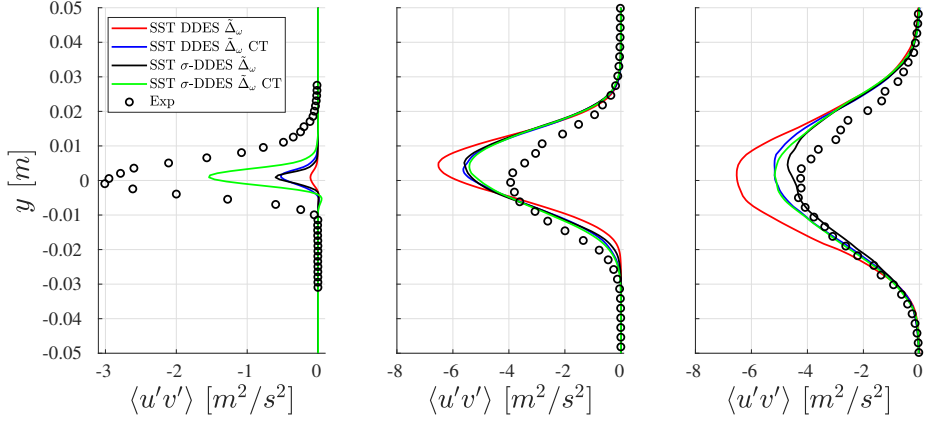


Figure 4.12: *Mixing shear layer flow using Hybrid RANS-LES SST-DDES. Commutation term is indicated by CT. Resolved shear stress at locations  $x = 0.2$  m (left),  $x = 0.65$  m (middle) and  $x = 0.95$  m (right). Results compared with experiment [100].*



# Chapter 5

## Summary of Papers

The main contribution and the major work done for each paper appended in the thesis are presented in this chapter. Comments are given to highlight possible improvement and future work.

### 5.1 Paper A

*"Investigation of Low-dissipation Low-dispersion Schemes for Incompressible and Compressible Flows in Scale-Resolving Simulations"*

In Paper A, a numerical scheme suitable for unstructured grids was investigated and developed. The numerical scheme is an essential part of a CFD code and will determine the capabilities of resolving the turbulent scales in the LES mode of hybrid RANS-LES. A low-dispersive, low-dissipative (LD2) scheme developed by Löwe et al. [42] and Probst et al. [43] was found suitable, since the scheme requires little modification to the second-order scalar valued Jameson-Schmidt-Turkel (JST) scheme already present in M-Edge. The scheme exploits a matrix valued dissipation operator to reduce the added numerical dissipation while maintaining numerical stability. Numerical dispersion is reduced and controlled by using higher order central reconstruction of the face values, using the local nodal gradients on each side of the cell face.

The work in Paper A is a continuation of the work in Carlsson et al. [74], in which the numerical scheme was evaluated in incompressible LES of the turbulent channel flow at  $Re_\tau = 395$  and decaying isotropic turbulence (DIT). In Paper A, the LD2 scheme was examined and modified for compressible flow cases involving shock discontinuities, LD2-Compressible (LD2C), and verified in a shock-tube problem. The scheme was then further verified in hybrid RANS-LES of DIT, and the turbulent channel flow for a wide range of Reynolds numbers in both subsonic and supersonic conditions. It is reported that the LD2C scheme can accurately predict the correct decay of the turbulent energy spectrum in DIT and the mean velocity profile and turbulent stresses in the turbulent channel flow cases.

Moreover, a supersonic base flow was simulated using hybrid RANS-LES. The LD2C scheme exploits a shock sensor incorporating vorticity and was shown to improve the prediction of the resolved shear stress in the shear layer of compression in comparison with the conventional scheme. However, the predicted base pressure was shown to be underestimated in comparison with experiments, which was also reported in the works by Simone et al. [92] and Guseva et al. [91]. This was caused by an overprediction of the back flow inside the recirculation bubble.

## 5.2 Paper B

*"Turbulence Injection Methods at RANS-LES Interfaces or Inlets for Scale-Resolving Simulations"*

The purpose of Paper B was to develop and demonstrate a methodology for injecting synthetic turbulence in a fully coupled embedded hybrid RANS-LES. Three different methods for imposing velocity fluctuations in a compressible finite-volume solver were evaluated for zonal hybrid RANS-LES applications using the SA-IDDES model. The methods were derived from an expansion of the governing equations, resulting in additional source terms stemming from the time derivative, the convective operator and a combination thereof. Additionally, following the work by Hamba [20], a commutation term was derived for the convection term in the SA turbulence model in order to rapidly reduce the turbulent viscosity across the RANS-LES interface. The three injection methods and the commutation term were verified in embedded RANS-LES using SA-IDDES in a turbulent channel flow at  $Re_\tau = 5200$  and zero-pressure-gradient boundary layer flow at  $Re_\theta \geq 3000$ , where the synthetic fluctuations were computed according to the Synthetic Turbulence Generator (STG) formulation by Shur et al. [28].

It is reported that the commutation term is able to effectively reduce the upstream RANS levels of turbulent viscosity to LES levels of turbulent viscosity across the embedded interface for both considered cases. The transition occurs over a distance much shorter than  $\delta$ , where  $\delta$  is the channel half width or the local boundary layer thickness. The formulation is expressed as a source term, and is free from model dependent parameters.

It is concluded that all the three injection methods perform very well for the turbulent channel flow case, and are able to reproduce reference simulation friction velocity (within a 5% margin) within  $1\delta$  downstream from the interface. In the simulations of the boundary layer flow, the discrepancy between the different injection methods are relatively large. The shortest recovery length with a well predicted skin friction level is produced by the combined approach. The other two approaches yield similar recovery lengths, considerably longer compared to the combined approach. However, all the simulations that are presented predict a skin friction distribution within 5% compared to the Coles-Fernholz correlation, which is used as a reference. Good agreement with DNS data further downstream is achieved for all simulation, with respect to mean velocity profile and resolved Reynolds stresses.

## 5.3 Paper C

*"Higher-Order Gradients on Unstructured Meshes Using Compact Formulation for Node-Centered Schemes"*

In Paper C, a new approach for gradient computations on node-centered unstructured grids was introduced. This was done in order to improve the numerical scheme in Paper A, which use nodal gradient for reconstructing the cell face values in the convective flux computations. The proposed approach derives a gradient algorithm from a least squares

(LSQ) approximation, where a local equation system is solved to introduce connectivity between neighbouring nodes. The resulting scheme forms a globally coupled linear system of equations for the gradients. The implicit LSQ (ILSQ) allows a higher-order gradient reconstruction using a compact formulation, i.e. using only nearest neighbours. This may greatly simplify implementations of higher-order schemes in unstructured CFD codes.

The ILSQ scheme was assessed in the capability of reconstructing the gradient of a known analytical function, and was implemented in a standalone MATLAB script. It is reported that the ILSQ scheme shows a fourth-order scaling on all grids considered, including highly irregular quadrilateral grids, triangular grids, mixed element grids and high-aspect-ratio grids ( $AR = 2000$ ). Using the same compact stencil, it is shown that a standard distance weighted explicit LSQ (ELSQ) can at most achieve a second-order scaling.

## Comments

The new gradient-reconstruction algorithm in Paper C considers only interior nodes and it was assumed that the gradient was known on the boundaries, i.e. a Neumann boundary condition. The proposed gradient scheme needs to be closed with a suitable boundary condition for cases when the gradient is unknown, e.g. a Dirichlet boundary condition, in order to maintain the fourth-order accuracy and be applicable for general CFD purposes.

While the overall accuracy of the numerical scheme in Paper A may be improved using the new gradient reconstruction scheme, a higher-order evaluation of the surface integral in the flux evaluation needs to be considered in order to raise the overall order of accuracy of a finite-volume scheme, as is shown by Gooch [93]. This can e.g. be achieved by using additional quadrature points in the surface integral [93] or an iterative k-exact reconstruction strategy by Setzwein et al. [101].

## 5.4 Paper D

*"Seamless Interface Methods for Grey-Area Mitigation in Scale-Resolving Hybrid RANS-LES"*

A new Grey-Area Mitigation (GAM) method was proposed in Paper D. A commutation residue term formulation by Girimaji and Wallin [21] for PANS modeling was further expanded to DES-type modeling aiming for a more rapid transition between modeled and resolved turbulent scales in the vicinity of a RANS-LES interface. The proposed GAM method, aiming to mitigate the grey area over the RANS-LES interface, is based on a commutation term stemming from the variation of the local hybrid length scale. Furthermore, a sub-grid model enabling to reduce the eddy viscosity in a shear layer, the  $\sigma$ -DDES model by Mocket et al [99], was also evaluated. Both methods require no additional manipulation of, or explicitly defining, the RANS-LES interface and are applied in a global manner.

Paper D reports hybrid RANS-LES computations undertaken in the verification of GAM formulations incorporated into the SST DDES model. Two test cases, namely, the flow over a wall-mounted hump and a mixing shear layer was computed. It was shown

that the effect of both the commutation term and the  $\sigma - DDES$  model improve the results for the mixing shear layer and are able to trigger a rapid transition of modeled to resolved turbulence. This indicated improved predictions of both vorticity thickness and resolved shear stress. The effect of commutation term and the  $\sigma - DDES$  model is less pronounced for the hump flow, however, where the recovery of the skin friction coefficient is only slightly better predicted.

## Comments

The commutation term presented in Paper D effectively reduces the modeled kinetic energy and eddy viscosity further in the vicinity of a RANS-LES interface. We believe that this is necessary but not enough, and synthetic turbulence could be added to further mitigate the grey area in flow cases where resolved fluctuations are not triggered by strong shear. The commutation term, which is a measure of the energy transfer between the modeled and resolved scales, can be used to scale the intensity of the synthetic fluctuations. The Anisotropic Linear Forcing (ALF) method by de Laage de Meux et al. [102] offers an interesting combination with the commutation term, due to its relatively small computational overhead, which is necessary since the commutation term is computed in the entire computational domain, and that it requires no explicit RANS-LES interface to be defined.

## 5.5 Paper E

*"Implementation of Nonreflecting Inlet and Outlet Boundary Conditions in the Subsonic Regime for a Node-Based Compressible Solver"*

With the experience gained from the work in Paper B, it was concluded that synthetic turbulent fluctuations may produce spurious pressure reflections in the vicinity of inlet or outlet boundaries. This is caused by an improper treatment of the incoming and outgoing characteristic waves at truncated computational domains, which is not accounted for in standard inlet/outlet boundary conditions. Paper E presents a survey on the implementation of the Navier-Stokes characteristic boundary conditions (NSCBC) by Lele et al. [103]. Special attention paid to node-centered finite volume schemes, with the aim to mitigate the reflected waves from the boundaries. Two different implementations were investigated of the NSCBC, the first sets the primitive variables at the boundary from the NSCBC equations, the other implements the NSCBC as a source term. The NSCBC implementations were compared to conventional boundary conditions.

A subsonic inlet was tested to evaluate the boundary conditions in their capability to inject an analytical isentropic vortex. The boundary conditions was verified in examining how well the analytical solution is preserved. A Dirichlet boundary condition was capable of injecting the vortex with minimal distortion and give accurate results. The strong implementation of setting the primitive variables at the boundary was capable of injecting the vortex, although significant checkerboard pattern is observed in the pressure. The source term implementation failed to inject the vortex in a reasonable form unless a high value of a penalty parameter  $\sigma$  is chosen. The value had to be chosen much larger than

the recommended value (50 vs. 0.25), although a zero value of this parameter has been reported in the literature to give satisfactory results.

A subsonic outlet was evaluated to assess the boundary conditions of their capability of transporting out an analytical vortex through the exit boundary. No reflections and minimal distortion of the vortex condition is expected. The NSCBC was compared to a conventional outlet condition with a static pressure specified. The static pressure outlet condition is reflective, and reflection in the pressure field is observed. The source term implementation of the NSCBC gives the best result with minimal reflections observed. The strong implementation of setting the primitive variables manages to transport out the vortex with checkerboard pattern observed.



# Chapter 6

## Conclusions and Outlook

The thesis work has dedicated to improvements of modelling and simulation methodologies for robust use in scale-resolving computations of turbulent flows of industry relevance. These concern of developing and examining both improved modelling approaches and feasible modelling-related numerical issues.

### 6.1 Concluding Remarks

A low-dissipative low-dispersive scheme (LD2) by Löwe et al. has been investigated in order to reduce the dissipative and dispersive numerical errors connected to the convective term. The scheme controls added artificial dissipation through a matrix dissipation operator and is adapted to low speed flows with a low Mach number preconditioner. The scheme exploits a higher order central reconstruction of the face fluxes to reduce the dispersive numerical error. In Paper A, the numerical scheme was applied in hybrid RANS-LES of turbulent channel flow and the decaying isotropic turbulence (DIT) for calibration purposes. The scheme was then further adopted to and assessed in compressible flows involving shock waves, such a shock tube case. Additional hybrid RANS-LES of supersonic flow over a cylindrical base further verifies the scheme and give good agreement with reference data.

A sensitivity study on the implementation of the Synthetic-Eddy Method (SEM) and the Synthetic Turbulence Generator (STG), to inject synthetic turbulence at the RANS-LES interface in order to mitigate the grey-area problem in the LES region has been made. Three methods have been implemented in Paper B, where the synthetic turbulent fluctuations is numerically represented by means of, respectively, a volumetric source term or a virtual flux term, or the combination of both methods, where the three methods were implemented through imposing the fluctuations (in the form of a source term) at the inlet boundary or in a plane further downstream of the inlet boundary. The methods have been verified in hybrid RANS-LES of developing turbulent channel flow and developing boundary layer.

In Paper C, an implicit least squares gradient (ILSQ) reconstruction scheme with a compact formulation has been derived. A detailed study of two-dimensional gradient calculation for node-centered unstructured data on regular and highly irregular grids has been made. Compared to a standard compact LSQ scheme, which uses only nearest neighbours in the stencil, the implicit scheme also includes information from neighbouring gradients, leading to a linear system to be solved. This allows the assumed polynomial or Taylor expansion in the least squares approach to be of higher order. In this study, a third-order polynomial is assumed for the ILSQ scheme. The ILSQ shows a fourth-order scaling on highly irregular mixed-element grids (quadrilaterals and triangles) with large variation in number of nearest neighbours.

In Paper D, a new seamless hybrid RANS-LES approach was derived and evaluated for free shear layer flows. The method exploits the commutation error at RANS-LES

interfaces, where a commutation error term based on the hybrid length-scale is applied to reduce the grey-area in the vicinity of the RANS-LES interface. Improved results with respect to experiment is achieved in hybrid RANS-LES of the mixing shear layer flow.

The Navier-Stokes characteristic boundary conditions (NSCBC) has been implemented in Paper E and evaluated in order to reduce numerical and physical wave reflections from simulation boundaries. The implementation was assessed by the transport of an analytical vortex in the subsonic regime. The current implementation of the boundary condition give satisfactory results for a subsonic outlet, where the vortex is effectively transported with minimal reflections. For a subsonic inlet, the implementation deviates from results reported in the literature and will be further examined.

The numerical scheme, the synthetic turbulence generator, and the characteristic boundary conditions were implemented and evaluated in M-Edge, a node-centered second-order unstructured compressible finite-volume Navier-Stokes solver. The new gradients scheme was implemented in a stand-alone script, where an implementation of the gradient scheme in the aforementioned flow solver is planned.

## 6.2 Outlook

The work presented in this thesis and in the appended papers is by no means considered the end of research effort dedicated to these topics. The numerical scheme will be further assessed and improved in verification and validation of additional hybrid RANS-LES flow cases. The performance of the numerical scheme will be examined and evaluated on true unstructured grids, i.e. grids containing mixed elements of hexahedra, prisms and tetrahedrons, which often is encountered in industrial applications of complex aeronautical flow cases.

The implementation of the characteristic boundary conditions will be further explored. A combination of the synthetic turbulent inlet boundary condition and the characteristic boundary condition is of special interest. The ability to inject synthetic turbulence while not producing unphysical pressure waves and reflections will be examined.

The current study of the new gradient-reconstruction algorithm is planned to be followed up by an implementation in the M-Edge flow solver, where the accuracy, feasibility and robustness will be further evaluated on relevant flow cases. The gradient scheme will be extended to three dimensions and applied to scale-resolving simulations for hybrid RANS-LES applications.

## References

- [1] *European Aviation: A vision for 2020*. [acare4europe.org](http://acare4europe.org).
- [2] European Commission, Directorate-General for Mobility, Transport, Directorate-General for Research, and Innovation. *Flightpath 2050 : Europe's vision for aviation : maintaining global leadership and serving society's needs*. Publications Office, 2011. DOI: [doi/10.2777/50266](https://doi.org/10.2777/50266).
- [3] Jeffrey P. Slotnick, A. Khodadoust, J. Alonso, D. Darmofal, W. Gropp, Elizabeth Lurie, and D. Mavriplis. "CFD Vision 2030 Study: A Path to Revolutionary Computational Aerosciences, NASA/CR-2014-218178". 2014.
- [4] P. Spalart, W-H Jou, M. Strelets, and S. Allmaras. "Comments on the Feasibility of LES for Wings, and on a Hybrid RANS/LES Approach". *Advanced in DNS/LES*. Jan. 1997.
- [5] A. Travin, M. Shur, M. Strelets, and P. Spalart. Detached-Eddy Simulations Past a Circular Cylinder. *Flow Turbulence and Combustion* **63** (Jan. 2000), 293–313. DOI: [10.1023/A:1009901401183](https://doi.org/10.1023/A:1009901401183).
- [6] P.R Spalart. Strategies for turbulence modelling and simulations. *International Journal of Heat and Fluid Flow* **21.3** (2000), 252–263. DOI: [https://doi.org/10.1016/S0142-727X\(00\)00007-2](https://doi.org/10.1016/S0142-727X(00)00007-2).
- [7] P. Spalart, S. Deck, M. Shur, K. Squires, M. Strelets, and A. Travin. A New Version of Detached-eddy Simulation, Resistant to Ambiguous Grid Densities. *Theoretical and Computational Fluid Dynamics* **20** (July 2006), 181–195. DOI: [10.1007/s00162-006-0015-0](https://doi.org/10.1007/s00162-006-0015-0).
- [8] M. L. Shur, P. R. Spalart, M. Kh. Strelets, and A. K. Travin. A hybrid RANS-LES approach with delayed-DES and wall-modelled LES capabilities. *International Journal of Heat and Fluid Flow* **29.6** (2008), 1638–1649. ISSN: 0142-727X. DOI: <https://doi.org/10.1016/j.ijheatfluidflow.2008.07.001>.
- [9] R. Schiestel and A. Dejoan. Towards a new partially integrated transport model for coarse grid and unsteady turbulent flow simulation. *Theoretical and Computational Fluid Dynamics* **18(6)** (2005), 443–468.
- [10] B. Chaouat and R. Schiestel. Progress in subgrid-scale transport modelling for continuous hybrid non-zonal RANS/LES simulations. *International Journal of Heat and Fluid Flow* **30.4** (2009), 602–616. ISSN: 0142-727X. DOI: <https://doi.org/10.1016/j.ijheatfluidflow.2009.02.021>.
- [11] *PANS Turbulence Model for Seamless Transition Between RANS and LES: Fixed-Point Analysis and Preliminary Results*. Vol. Volume 2: Symposia, Parts A, B, and C. Fluids Engineering Division Summer Meeting. July 2003, pp. 1901–1909.
- [12] S. S. Girimaji. Partially-Averaged Navier-Stokes Model for Turbulence: A Reynolds-Averaged Navier-Stokes to Direct Numerical Simulation Bridging Method. *Journal of Applied Mechanics* **73.3** (Nov. 2005), 413–421.
- [13] Florian M. and Yury E. "A Scale Adaptive Simulation Model using Two-Equation Models". *43rd AIAA Aerospace Sciences Meeting and Exhibit*. DOI: [10.2514/6.2005-1095](https://doi.org/10.2514/6.2005-1095).

- [14] S. H. Peng. Hybrid RANS-LES modeling based on zero- and one-equation models for turbulent flow simulation. *4th International Symposium on Turbulence and Shear Flow Phenomena* **3** (Jan. 2005), 1159–1164.
- [15] S. H. Peng. “Algebraic Hybrid RANS-LES Modelling Applied to Incompressible and Compressible Turbulent Flows”. Vol. 4. June 2006. DOI: [10.2514/6.2006-3910](https://doi.org/10.2514/6.2006-3910).
- [16] Sébastien Deck. Recent improvements in the Zonal Detached Eddy Simulation (ZDES) formulation. *Theoretical and Computational Fluid Dynamics* **26** (Dec. 2011), 1–28. DOI: [10.1007/s00162-011-0240-z](https://doi.org/10.1007/s00162-011-0240-z).
- [17] Sébastien Deck and Nicolas Renard. Towards an enhanced protection of attached boundary layers in hybrid RANS/LES methods. *Journal of Computational Physics* **400** (2020), 108970. ISSN: 0021-9991. DOI: <https://doi.org/10.1016/j.jcp.2019.108970>.
- [18] Tabor G. Fureby C. Mathematical and Physical Constraints on Large-Eddy Simulations. *Theoretical Computation Fluid Dynamics* **9** (1997), 85–102. DOI: <https://doi.org/10.1007/s001620050034>.
- [19] M. Germano. Properties of the hybrid RANS/LES filter. *Theoretical Computation Fluid Dynamics* **17** (2004), 225–231. DOI: <https://doi.org/10.1007/s00162-004-0116-6>.
- [20] Fujihira Hamba. Analysis of filtered Navier–Stokes equation for hybrid RANS/LES simulation. *Physics of Fluids* **23.1** (2011), 015108.
- [21] Sharath S. Girimaji and Stefan Wallin. Closure modeling in bridging regions of variable-resolution (VR) turbulence computations. *Journal of Turbulence* **14.1** (2013), 72–98. DOI: [10.1080/14685248.2012.754893](https://doi.org/10.1080/14685248.2012.754893).
- [22] L. Davidson. Zonal PANS: evaluation of different treatments of the RANS–LES interface. *Journal of Turbulence* **17.3** (2016), 274–307.
- [23] L. Davidson. Two-equation hybrid RANS–LES models: a novel way to treat k and at inlets and at embedded interfaces. *Journal of Turbulence* **18.4** (2017), 291–315.
- [24] S. Arvidson, L. Davidson, and S.-H. Peng. Interface methods for grey-area mitigation in turbulence-resolving hybrid RANS-LES. *International Journal of Heat and Fluid Flow* **73** (2018), 236–257. ISSN: 0142-727X. DOI: <https://doi.org/10.1016/j.ijheatfluidflow.2018.08.005>.
- [25] Nitin S. Dhamankar, Gregory A. Blaisdell, and Anastasios S. Lyrintzis. Overview of Turbulent Inflow Boundary Conditions for Large-Eddy Simulations. *AIAA Journal* **56.4** (2018), 1317–1334. DOI: [10.2514/1.J055528](https://doi.org/10.2514/1.J055528).
- [26] Robert H. Kraichnan. Diffusion by a Random Velocity Field. *Physics of Fluids* **13** (1970), 22–31. DOI: [10.1063/1.1692799](https://doi.org/10.1063/1.1692799).
- [27] P. Batten, U. Goldberg, and S. Chakravarthy. Interfacing Statistical Turbulence Closures with Large-Eddy Simulation. *AIAA Journal* **42.3** (2004), 485–492. DOI: [10.2514/1.3496](https://doi.org/10.2514/1.3496).
- [28] M.L. Shur, P.R. Spalart, M.K. Strelets, and A.K. Travin. Synthetic Turbulence Generators for RANS-LES Interfaces in Zonal Simulations of Aerodynamic and Aeroacoustic Problems. *Flow, Turbulence and Combustion* **93** (2014), 63–92. DOI: [10.1007/s10494-014-9534-8](https://doi.org/10.1007/s10494-014-9534-8).

- [29] L. Davidson and M. Billson. Hybrid LES-RANS using synthesized turbulent fluctuations for forcing in the interface region. *International Journal of Heat and Fluid Flow* **27** (2006), 1028–1042.
- [30] N. Jarrin, S. Benhamadouche, D. Laurance, and R. Prosser. A synthetic-eddy-method for generating inflow conditions for large-eddy simulations. *International Journal of Heat and Fluid Flow* **27** (2006), 585–593.
- [31] N. Jarrin, R. Prosser, J.-C. Uribe, S. Benhamadouche, and D. Laurance. Reconstruction of turbulent fluctuations for hybrid RANS/LES simulations using a Synthetic-Eddy Method. *International Journal of Heat and Fluid Flow* **30** (2009), 435–442.
- [32] R. Poletto, A. Revell, T. Craft, and N. Jarrin. Divergence free synthetic eddy method for embedded LES inflow boundary conditions. *Seventh international Symposium On Turbulence and Shear Flow Phenomena (TSFP-7)* (2011).
- [33] A. Skillen, A. Revell, and T. Craft. Accuracy and efficiency improvements in synthetic eddy methods. *International Journal of Heat and Fluid Flow* **62** (2016), 386–394. DOI: <https://doi.org/10.1016/j.ijheatfluidflow.2016.09.008>.
- [34] X.-D. Liu, S. Osher, and T. Chan. Weighted Essentially Non-oscillatory Schemes. *Journal of Computational Physics* **115.1** (1994), 200–212. ISSN: 0021-9991. DOI: <https://doi.org/10.1006/jcph.1994.1187>.
- [35] R. Abgrall. On Essentially Non-oscillatory Schemes on Unstructured Meshes: Analysis and Implementation. *Journal of Computational Physics* **114.1** (1994), 45–58. ISSN: 0021-9991. DOI: <https://doi.org/10.1006/jcph.1994.1148>.
- [36] B. Cockburn and C.-W. Shu. TVB Runge-Kutta Local Projection Discontinuous Galerkin Finite Element Method for Conservation Laws II: General Framework. *Mathematics of Computation* **52.186** (1989), 411–435. ISSN: 00255718, 10886842.
- [37] Z.J. Wang. Spectral (Finite) Volume Method for Conservation Laws on Unstructured Grids. Basic Formulation: Basic Formulation. *Journal of Computational Physics* **178.1** (2002), 210–251. ISSN: 0021-9991. DOI: <https://doi.org/10.1006/jcph.2002.7041>.
- [38] Z.J. Wang and Yen Liu. Spectral (Finite) Volume Method for Conservation Laws on Unstructured Grids: II. Extension to Two-Dimensional Scalar Equation. *Journal of Computational Physics* **179.2** (2002), 665–697. ISSN: 0021-9991. DOI: <https://doi.org/10.1006/jcph.2002.7082>.
- [39] Y. Liu, M. Vinokur, and Z. J. Wang. “Discontinuous Spectral Difference Method for Conservation Laws on Unstructured Grids”. *Computational Fluid Dynamics 2004*. Ed. by C. Groth and D. W. Zingg. Berlin, Heidelberg: Springer Berlin Heidelberg, 2006, pp. 449–454.
- [40] G. Lodato, P. Castonguay, and A. Jameson. Structural Wall-modeled LES Using a High-order Spectral Difference Scheme for Unstructured Meshes. *Flow, Turbulence and Combustion* **92.1-2** (Jan. 2014). WOS:000328844400028, 579–606. DOI: 10.1007/s10494-013-9523-3.
- [41] A. Probst and S. Reuß. “Scale-Resolving Simulations of Wall-Bounded Flows with an Unstructured Compressible Flow Solver”. *Progress in Hybrid RANS-LES Modelling*. Vol. 130. Springer, 2015, pp. 481–491.

- [42] J. Löwe, A. Probst, T. Knopp, and R. Kessler. Low-Dissipation Low-Dispersion Second-Order Scheme for Unstructured Finite-Volume Flow Solvers. *AIAA Journal* **54** (2016). DOI: 10.2514/1.J054956.
- [43] Axel Probst, Johannes Löwe, Silvia Probst, Tobias Knopp, and Roland Kessler. Scale-Resolving Simulations with a Low-Dissipation Low-Dispersion Second-Order Scheme for Unstructured Flow Solvers. *AIAA Journal* **54** (July 2016), 1–15. DOI: 10.2514/1.J054957.
- [44] A. Jameson. Time-dependent calculations using multigrid with applications to unsteady flows past airfoils and wings. *AIAA Paper* 91-1596 (1991).
- [45] F Ducros, Valerie Ferrand, Nicoud Franck, C Weber, Denis Darracq, C Gacherieu, and Thierry Poinso. LES of the Shock/Turbulence Interaction. *Journal of Computational Physics* **152** (July 1999), 517–549. DOI: 10.1006/jcph.1999.6238.
- [46] P.R Spalart. Strategies for turbulence modelling and simulations. *International Journal of Heat and Fluid Flow* **21.3** (2000), 252–263. ISSN: 0142-727X. DOI: [https://doi.org/10.1016/S0142-727X\(00\)00007-2](https://doi.org/10.1016/S0142-727X(00)00007-2).
- [47] A. Favré. “Problems of Hydrodynamics and Continuum Mechanics”. *Society for Industrial and Applied Mathematics*. 1969, pp. 231–266.
- [48] P. Spalart and S. Allmaras. “A one-equation turbulence model for aerodynamic flows”. *30th Aerospace Sciences Meeting and Exhibit*. DOI: 10.2514/6.1992-439.
- [49] B. Aupoix and P.R. Spalart. Extensions of the Spalart–Allmaras turbulence model to account for wall roughness. *International Journal of Heat and Fluid Flow* **24.4** (2003). Selected Papers from the Fifth International Conference on Engineering Turbulence Modelling and Measurements, 454–462. ISSN: 0142-727X.
- [50] Florian Menter, M. Kuntz, and RB Langtry. Ten years of industrial experience with the SST turbulence model. *Heat and Mass Transfer* **4** (Jan. 2003).
- [51] W.P Jones and Brian Launder. The prediction of laminarization with a two-equation model of turbulence. *International Journal of Heat and Mass Transfer* **15** (Feb. 1972), 301–314. DOI: 10.1016/0017-9310(72)90076-2.
- [52] D. Wilcox. *Turbulence Modeling for CFD (Third Edition)*. Jan. 2006.
- [53] J. Smagorinsky. General circulation experiments with the primitive equations: I. The basic experiment. *Monthly Weather Review* **91.3** (Mar. 1963), 99–164. DOI: 10.1175/1520-0493(1963)091<0099:GCEWTP>2.3.CO;2.
- [54] F. Nicoud and F. Ducros. Subgrid-scale stress modelling based on the square of the velocity gradient tensor. *Flow, Turbulence and Combustion* **63** (1999), 183–200.
- [55] Franck Nicoud, Hubert Baya Toda, Olivier Cabrit, Sanjeeb Bose, and Jungil Lee. Using singular values to build a subgrid-scale model for large eddy simulations. *Physics of Fluids* **23.8** (2011), 085106. DOI: 10.1063/1.3623274.
- [56] P. Spalart, W-H Jou, M. Strelets, and S. Allmaras. “Comments on the Feasibility of LES for Wings, and on a Hybrid RANS/LES Approach”. Jan. 1997, pp. 137–147.
- [57] Mikhail Gritskevich, Andrey Garbaruk, Jochen Schütze, and Florian Menter. Development of DDES and IDDES Formulations for the k- Shear Stress Transport Model. *Flow, Turbulence and Combustion* **88** (Apr. 2012). DOI: 10.1007/s10494-011-9378-4.

- [58] Michael Shur, Philippe Spalart, Michael Strelets, and Andrey Travin. An Enhanced Version of DES with Rapid Transition from RANS to LES in Separated Flows. *Flow, Turbulence and Combustion* **95** (Dec. 2015). DOI: [10.1007/s10494-015-9618-0](https://doi.org/10.1007/s10494-015-9618-0).
- [59] Thomas S. Lund, Xiaohua Wu, and Kyle D. Squires. Generation of Turbulent Inflow Data for Spatially-Developing Boundary Layer Simulations. *Journal of Computational Physics* **140.2** (1998), 233–258. ISSN: 0021-9991. DOI: <https://doi.org/10.1006/jcph.1998.5882>.
- [60] M. Carlsson, L. Davidson, S.H. Peng, and S. Arvidson. “Investigation of Turbulence Injection Methods in Compressible Flow Solvers in Large Eddy Simulation”. *2022 AIAA SciTech Forum*. Jan. 2022. DOI: [10.2514/6.2022-0483](https://doi.org/10.2514/6.2022-0483).
- [61] F. Mathey. Aerodynamic noise simulation of the flow past an airfoil trailing-edge using a hybrid zonal RANS-LES. *Computers & Fluids* **37** (2007), 836–843.
- [62] S. Schmidt and M Breuer. Source term based synthetic turbulence inflow generator for eddy-resolving predictions of an airfoil flow including a laminar separation bubble. *Computer & Fluids* **146** (2017), 1–22.
- [63] A. Probst. Implementation and assesment of the Synthetic-Eddy Method in an unstructured compressible flow solver. *Progress in Hybrid RANS-LES Modelling. NFMMD* **137** (2018), 91–101.
- [64] Donald P. Rizzetta and Daniel J. Garmann. Wall-Resolved Large-Eddy Simulation of Smooth-Body Separated Flow. *International Journal of Computational Fluid Dynamics* **36.1** (2022), 1–20. DOI: [10.1080/10618562.2022.2087873](https://doi.org/10.1080/10618562.2022.2087873).
- [65] M. Carlsson, S. Wallin, L. Davidson, S.H. Peng, and S. Arvidson. “Seamless Interface Methods for Grey-Area Mitigation in Scale-Resolving Hybrid RANS-LES”. *DLES13 2022*. 2022.
- [66] P. Eliasson. “Edge, a Navier–Stokes solver for unstructured grids”. *Finite Volumes for Complex Applications*. Vol. III. CP849. 2002, pp. 527–534.
- [67] P. Eliasson and P. Weinerfelt. “Recent applications of the flow solver Edge”. *7th Asian CFD Conference*. CP849. 2007.
- [68] J. C. Kok. A high-order low-dispersion symmetry-preserving finite volume method for compressible flow on curvilinear grids. *Journal of Computational Physics* **228** (2009), 6811–6832. DOI: <https://doi.org/10.1016/j.jcp.2009.06.015>.
- [69] R. C. Swanson and E. Turkel. On the central-difference and upwind schemes. *Journal of Computational Physics* **101** (1992), 292–306. DOI: [https://doi.org/10.1016/0021-9991\(92\)90007-L](https://doi.org/10.1016/0021-9991(92)90007-L).
- [70] Antony Jameson. Origins and Further Development of the Jameson–Schmidt–Turbel Scheme. *AIAA Journal* **55.5** (2017), 1487–1510. DOI: [10.2514/1.J055493](https://doi.org/10.2514/1.J055493).
- [71] P. Eliasson, S. Eriksson, and J. Nordström. The influence of weak and strong solid wall boundary conditions on the convergence to steady-state of the navier-stokes equations. *AIAA Paper* 2009-3551 (2009).
- [72] A. Jameson, W. Schmidt, and E. Turkel. “Numerical solution of the Euler equations by finite volume methods using Runge Kutta time stepping schemes”. *14th Fluid and Plasma Dynamics Conference*. 1981. DOI: [10.2514/6.1981-1259](https://doi.org/10.2514/6.1981-1259).
- [73] S. Langer. Investigations of a compressible second order finite volume code towards the incompressible limit. *Computer and Fluids* **149** (2017), 119–137.

- [74] M. Carlsson, L. Davidson, S.H. Peng, and S. Arvidson. “Parametric Investigation of Low-dissipation Low-dispersion Schemes for Unstructured Flow Solvers in Large Eddy Simulation”. *2020 AIAA SciTech Forum*. 2020.
- [75] S. K. Godunov and I. Bohachevsky. Finite difference method for numerical computation of discontinuous solutions of the equations of fluid dynamics. *Matematičeskij sbornik* **47(89)**.3 (1959), 271–306.
- [76] E. Turkel, R. Radespiel, and N. Kroll. Assessment of preconditioning methods for multidimensional aerodynamics. *Computer and Fluids* **26** (1997), 613–643. DOI: [https://doi.org/10.1016/S0045-7930\(97\)00013-3](https://doi.org/10.1016/S0045-7930(97)00013-3).
- [77] M. Carlsson, L. Davidson, S.H. Peng, and S. Arvidson. “Higher Order Gradients on Unstructured Meshes Using Compact Formulation for Node-Centered Schemes”. *2022 AIAA Aviation Forum*. June 2022. DOI: [10.2514/6.2022-4156](https://doi.org/10.2514/6.2022-4156).
- [78] Dimitri Mavriplis. “Revisiting the Least-Squares Procedure for Gradient Reconstruction on Unstructured Meshes”. *16th AIAA Computational Fluid Dynamics Conference*. DOI: [10.2514/6.2003-3986](https://doi.org/10.2514/6.2003-3986).
- [79] Fan Zhang. *A vertex-weighted-Least-Squares gradient reconstruction*. 2017. DOI: [10.48550/ARXIV.1702.04518](https://doi.org/10.48550/ARXIV.1702.04518).
- [80] Hiroaki Nishikawa and Jeffery A. White. An efficient cell-centered finite-volume method with face-averaged nodal-gradients for triangular grids. *Journal of Computational Physics* **411** (2020), 109423. ISSN: 0021-9991. DOI: <https://doi.org/10.1016/j.jcp.2020.109423>.
- [81] Hong Luo, Joseph D. Baum, and Rainald Löhner. A discontinuous Galerkin method based on a Taylor basis for the compressible flows on arbitrary grids. *Journal of Computational Physics* **227**.20 (2008), 8875–8893. ISSN: 0021-9991. DOI: <https://doi.org/10.1016/j.jcp.2008.06.035>.
- [82] G. Comte-Bellot and S. Corrsin. Simple eulerian time correlation of full- and narrow-band velocity signals in grid-generated "isotropic" turbulence. *Journal of Fluid Mechanics* **48** (1971), 943–13. DOI: [10.1017/S0022112071001599](https://doi.org/10.1017/S0022112071001599).
- [83] E. Fares and W. Schröder. A general one-equation turbulence model for free shear and wall-bounded flows. *Flow, Turbulence and Combustion* **73** (2005), 187–215. DOI: <https://doi.org/10.1007/s10494-005-8625-y>.
- [84] R. Moser, J. Kim, and N. Mansour. Direct numerical simulation of turbulent channel flow up to  $Re = 590$ . *Physics of Fluids* **11.4** (1999), 943–13. DOI: [10.1006/1.869966](https://doi.org/10.1006/1.869966).
- [85] Davide Modesti and Sergio Pirozzoli. Reynolds and Mach number effects in compressible turbulent channel flow. *International Journal of Heat and Fluid Flow* **59** (2016), 33–49. DOI: <https://doi.org/10.1016/j.ijheatfluidflow.2016.01.007>.
- [86] G. N. Coleman, J. Kim, and R. D. Moser. A numerical study of turbulent supersonic isothermal-wall channel flow. *Journal of Fluid Mechanics* **305** (1995), 159–183. DOI: [10.1017/S0022112095004587](https://doi.org/10.1017/S0022112095004587).
- [87] H. Reichardt. Vollständige Darstellung der turbulenten Geschwindigkeitsverteilung in glatten Leitungen. *ZAMM - Journal of Applied Mathematics and Mechanics / Zeitschrift für Angewandte Mathematik und Mechanik* **31.7** (1951), 208–219. DOI: <https://doi.org/10.1002/zamm.19510310704>.

- [88] E. R. Van Driest. Turbulent Boundary Layer in Compressible Fluids. *Journal of the Aeronautical Sciences* **18.3** (1951), 145–160. DOI: 10.2514/8.1895.
- [89] J. L. Herrin and J. C. Dutton. Supersonic base flow experiments in the near wake of a cylindrical afterbody. *AIAA Journal* **32.1** (1994), 77–83. DOI: 10.2514/3.11953.
- [90] Werner Haase, Marianna Braza, and Alistair Revell. *DESider: A European effort on hybrid RANS-LES Modelling (Notes on numerical fluid mechanics multidisciplinary design, Vol. 103)*. Vol. 103. Jan. 2009. ISBN: 978-3-540-92772-3. DOI: 10.1007/978-3-540-92773-0.
- [91] Ekaterina Guseva, Andrey Garbaruk, and Michael Strelets. Assessment of Delayed DES and Improved Delayed DES Combined with a Shear-Layer-Adapted Subgrid Length-Scale in Separated Flows. *Flow, Turbulence and Combustion* **98** (Mar. 2017). DOI: 10.1007/s10494-016-9769-7.
- [92] Franck Simon, Sébastien Deck, Philippe Guillen, and Pierre Sagaut. Reynolds-Averaged Navier-Stokes/Large-Eddy Simulations of Supersonic Base Flow. *AIAA Journal* **44.11** (2006), 2578–2590. DOI: 10.2514/1.21366.
- [93] C. Ollivier-Gooch, A. Nejat, and Krzysztof M. Obtaining and Verifying High-Order Unstructured Finite Volume Solutions to the Euler Equations. *AIAA Journal* **47.9** (2009), 2105–2120. DOI: 10.2514/1.40585.
- [94] H. Nishikawa. From hyperbolic diffusion scheme to gradient method: Implicit Green–Gauss gradients for unstructured grids. *Journal of Computational Physics* **372** (2018), 126–160. ISSN: 0021-9991. DOI: <https://doi.org/10.1016/j.jcp.2018.06.019>.
- [95] Charles Mocket, W Haase, and F Thiele. “Go4hybrid: An European Initiative for Improved Hybrid RANS-LES Modelling”. *Progress in Hybrid RANS-LES Modelling*. Ed. by S Girimaji, W Haase, Shia-Hui Peng, and Dieter Schwamborn. Vol. 130. Cham: Springer International Publishing, 2015, pp. 299–303.
- [96] Sébastien Deck, Pierre-Elie Weiss, and Nicolas Renard. A rapid and low noise switch from RANS to WMLES on curvilinear grids with compressible flow solvers. *Journal of Computational Physics* **363** (2018), 231–255. ISSN: 0021-9991. DOI: <https://doi.org/10.1016/j.jcp.2018.02.028>.
- [97] Hassan M Nagib, Kapil A Chauhan, and Peter A Monkewitz. Approach to an asymptotic state for zero pressure gradient turbulent boundary layers. *Philosophical Transactions of the Royal Society A: Mathematical, Physical and Engineering Sciences* **365**.1852 (2007), 755–770.
- [98] Philipp Schlatter and Ramis Örlü. Assessment of direct numerical simulation data of turbulent boundary layers. *Journal of Fluid Mechanics* **659** (Sept. 2010), 116–126.
- [99] Charles Mockett, Marian Fuchs, Andrey Garbaruk, Michael Shur, Philippe Spalart, Michael Strelets, Frank Thiele, and Andrey Travin. “Two Non-zonal Approaches to Accelerate RANS to LES Transition of Free Shear Layers in DES”. *Progress in Hybrid RANS-LES Modelling*. Ed. by Sharath Girimaji, Werner Haase, Shia-Hui Peng, and Dieter Schwamborn. Cham: Springer International Publishing, 2015, pp. 187–201. ISBN: 978-3-319-15141-0. DOI: [https://doi.org/10.1007/978-3-319-15141-0\\_15](https://doi.org/10.1007/978-3-319-15141-0_15).

- [100] Delville J. “La décomposition orthogonale aux valeurs propres et l’analyse de l’organisation tridimensionnelle des écoulements turbulents ci saillés libre”. PhD thesis. Université de Poitier, 1995.
- [101] Florian Setzwein, Peter Ess, and Peter Gerlinger. An implicit high-order k-exact finite-volume approach on vertex-centered unstructured grids for incompressible flows. *Journal of Computational Physics* **446** (2021), 110629. ISSN: 0021-9991. DOI: <https://doi.org/10.1016/j.jcp.2021.110629>.
- [102] B. de Laage de Meux, B. Audebert, R. Manceau, and R. Perrin. Anisotropic linear forcing for synthetic turbulence generation in large eddy simulation and hybrid RANS/LES modeling. *Physics of Fluids* **27.3** (2015), 035115. DOI: 10.1063/1.4916019.
- [103] Sanjiva K. Lele. Compact finite difference schemes with spectral-like resolution. *Journal of Computational Physics* **103.1** (1992), 16–42. ISSN: 0021-9991. DOI: [https://doi.org/10.1016/0021-9991\(92\)90324-R](https://doi.org/10.1016/0021-9991(92)90324-R).
- [104] M. Carlsson, L. Davidson, S.H. Peng, and S. Arvidson. “Investigation of Low-dissipation Low-dispersion Schemes for Incompressible and Compressible Flows in Scale-Resolving Simulations”. Submitted for journal publication.
- [105] M. Carlsson, L. Davidson, S.H. Peng, and S. Arvidson. *Implementation of Non-reflecting Inlet and Outlet Boundary Conditions in the Subsonic Regime for a Node-Based Compressible Solver*. Tech. rep. Chalmers University of Technology, Göteborg, Sweden, Technical Report, 2021.
- [106] S. Arvidson, M. Carlsson, and S. Nilsson. “Effect of LES Length Scale and Numerical Scheme in Hybrid RANS-LES of Free Shear Layer Flows”. *International Council of Aeronautical Sciences (ICAS), Stockholm*. 2022.